Fuel 335 (2023) 127018

Contents lists available at ScienceDirect

Fuel

journal homepage: www.elsevier.com/locate/fuel

Full length article

Effects of varying the liquid fuel type and air co-flow conditions on the microscopic spray characteristics in an atmospheric annular co-flow spray burner

Santiago Cardona [a,*], Raul Payri [b], F.J. Salvador [b], Jaime Gimeno [b]

[a] CCRC, King Abdullah University of Science and Technology (KAUST), Thuwal, 23955-6900, Saudi Arabia
[b] CMT-Motores Térmicos, Universitat Politècnica de València, Camino de Vera, s/n 46022 Valencia, Spain

ARTICLE INFO

Keywords:
Pressure-swirl atomizer
Spray characteristics
Sauter mean diameter
Microscopic Diffused Back-Illumination

ABSTRACT

The atomization process is critical for combustion systems since it directly influences emissions and performance. Thus injection system should provide the spray required structure and characteristics, e.g., angle and droplet size distribution. Therefore, this work investigates the effects of varying the fuel type, air co-flow rates, fuel mass flow rate and air co-flow temperature on the spray characteristics (e.g., droplet size distribution and droplet velocity) in an annular co-flow spray burner. These effects were investigated by measuring droplet sizes and velocities at different radial and axial positions of n-Heptane, n-Decane and n-Dodecane sprays under non-reacting conditions at a room pressure of 1 atm and temperature of 298 K and using the Microscopic Diffused Back-illumination (MDBI) technique. In addition, the Sauter mean diameter (SMD) for different flow conditions were predicted using three well-known correlations and compared to experimental measurements. The outcomes of this research provided a fair understanding of the influence of varying these parameters on the droplet sizes and velocity through a wide test matrix. Finally, the findings reported here will support future research into the function of phase change in flame stability.

1. Introduction

Developing efficient and clean combustion systems requires a deep understanding of all the processes experienced by liquid fuel throughout the system, such as atomization, vaporization, turbulent mixing, and combustion. Many of these processes are connected; the atomization process, which results in different droplet sizes, can increase or decrease the liquid fuel's vaporization rate and hence influencing the energy conversion process and pollutant emissions. Additionally, the combustion/flame stability of a liquid-fueled gas turbine can be affected by the fuel type and the air co-flow rates delivered in the engine. Increasing the fuel and/or air flow rates can improve droplet disintegration and flow turbulence, influencing the spray droplet size distribution. Therefore, the droplet formation in air flows must continue to be investigated because it is a complex process that is not fully understood yet. In the last decades, various experimental approaches and high-fidelity computational fluid dynamics (CFD) efforts have been used to understand the physical processes that drive the atomization process. Thus, reliable experimental measures are required to validate numerical modeling works [1–3] and are also used by designers to optimize new injection systems. Finally, accurate experimental data is necessary to understand the fuel droplet interaction with the flame structure through the evaporation and combustion steps.

In this context, several experimental investigations have been conducted to evaluate the influence of the fuel properties (e.g., density, surface tension and viscosity) on the atomization quality using different nozzle types [4–7]. Additional works have implemented analogous efforts on understanding the turbulent two-phase combustion in spray flames [8–11], since it continues to be a challenge for experiments and numerical simulations due to the complex interaction of the different mechanisms that are involved in them. Although many experiments have been conducted to investigate the relationship between the atomization process and the flame stability mechanism that occurs in spray flames, factors such as air co-flow, pre-heated and diluted co-flow, and fuel mass flow rates, which can influence droplet size distribution (DSD), velocity, and turbulence, require further investigation. Finally, one of the most basic requirements, particularly for aircraft engines, is the capacity to maintain combustion inside a gas turbine combustor under a wide range of operating conditions (e.g., fuel/air ratio, temperature, and pressure).

* Corresponding author.
E-mail address: santiago.vargas@kaust.edu.sa (S. Cardona).

https://doi.org/10.1016/j.fuel.2022.127018
Received 24 June 2022; Received in revised form 14 November 2022; Accepted 27 November 2022
Available online 14 December 2022

Nomenclature

Acronyms

CAD	Computer-aided design
CCD	Charge-Coupled Device
CFD	Computational fluid dynamics
DBI	Diffused Back-Illumination
DSD	Droplet size distribution
FOV	Fields of view
fps	Frames per second
GRT	Global Rainbow Refractometry Technique
LDV	Laser Doppler Velocimetry
LED	Light-emitting Diode
LEM	Laser Extinction Method
LII	Laser-Induced Incandescence
MDBI	Microscopic Diffused Back-Illumination
PDI	Phase Doppler Interferometry
PDPA	Phase Doppler Particle Analyzer
PID	Proportional Integral Derivative
PIV	Particle Image Velocimetry
PLIF	Planar Laser-induced Fluorescence
SEM	Scanning Electronic Microscope
SMD	Sauter Mean Diameter
TEM	Transmission Electron Microscope

Variables

μ_l	Dynamic viscosity
ν_l	Kinematic viscosity
ϕ_{global}	Global equivalence ratio
ρ_{air}	Air density
ρ_l	Fuel density
σ_l	Liquid surface tension
θ	Spray half-angle

Greek symbols

$\emptyset_{air}$	Air outlet diameter
d	Droplet diameter
N	Total number of valid droplets
$T_{co-flow}$	Air co-flow temperature
$V_{co-flow}$	Co-flow velocity

Experimental works of sprays surrounded by turbulent air co-flows were also carried out to measure droplet size distributions and velocities, but they are limited. Sommerfeld and Qiu [12] measured experimentally droplet sizes, distributions, velocities, and droplet mass fluxes of a hollow cone spray surrounded by heated co-flow using Phase Doppler Particle Analyzer (PDPA). The experiments were conducted at different flow conditions (i.e., varying air and liquid flow rates and air co-flow temperatures). The results exhibited that low air co-flow velocities compared to the droplet initial velocity increase the evaporation rate due to the more significant droplet interaction time (resident time) with the surrounding heated air. In addition, decreasing air co-flow velocity allows for a wider radial spray. Alsulami et al. [13] investigated the effect of varying the air flow rates on the spray characteristics (e.g., droplet size distribution) in an annular co-flow spray burner and using the PDPA technique. The droplet sizes and velocities of the spray were measured at different radial and axial positions of n-heptane fuel under non-reacting conditions. The outcomes evidenced that the spray characteristics, including droplet sizes, velocities, turbulence, and DSDs, are long influenced by the air co-flow rate and thus influence the droplet dissipation and vaporization.

Numerous optical and laser techniques have been developed for studying the spray's characteristics [14–19]. Friedman and Renksizbulut [14] used Phase Doppler Interferometry (PDI) to measure the fuel droplet size and velocity of a methanol spray in an annular air jet. This technique is based on measuring the phase difference and frequency of light scattered when a droplet passes through the intersection of two laser beams. Marley et al. [15] conducted experiments to determine the spray dispersion and aerodynamic properties of an ethanol spray using the PDPA and the Laser Doppler Velocimetry (LDV) techniques. Meanwhile, Düwel et al. [17] carried out experimental and numerical studies in a spray burner, where air and liquid fuel are injected at ambient temperature favoring direct droplet interaction. Experimental and computational results showed a good agreement in droplet velocities profiles and droplet size distribution. Verdier et al. [18] investigated an n-Heptane spray flame characteristics in an annular non-swirled air co-flow that surrounds a central hollow-cone spray injector using laser-based techniques. The PDPA measurements contributed to the analysis of air and droplet aerodynamics and the ones of the Global Rainbow Refractometry Technique (GRT) to investigate the droplet temperature in different regions of the spray jet. Subsequently, Marrero Santiago et al. [19] implemented PDA and Particle Image Velocimetry (PIV) to measure droplet size-velocity and instantaneous velocity fields in an n-Heptane spray, respectively.

Nowadays, Diffused Back-Illumination (DBI) has been widely used for measuring different parameters in sprays [20–27]. Yan et al. [28] investigated macroscopic and microscopic characteristics of flash boiling spray using Diffused Back-Illumination (DBI) imaging and PDA. Manin et al. [29] studied the mixing process in sprays at elevated temperatures and pressures using a high-speed camera coupled with a long-working-distance microscopy lens to track individual fluid features. Meanwhile, Payri et al. [22] determined the droplet size distribution of a urea–water spray injected into a hot air stream through the DBI technique, concluding that injection pressure plays an important role in the global spray performance; the droplet size and droplet velocity near the nozzle exit.

Pressure-swirl sprays are usually characterized to be quite dense with different sizes and shapes; thus, measuring them is a complex task [30]. Multiple scattering leads to a high level of noise and low contrast of images, even the detection of separate particles might be a problem. Therefore, choosing the appropriate optical technique that provides reliable information about the droplet size and velocity is very important. Microscopic Diffused Back-Illumination (MDBI) technique was used for this work since it allows for the spatial distribution of droplet size, allowing us to determine the droplet size and velocity. MDBI requires focused images and a short deep field appropriate for dense sprays. This work investigates the impact of varying the fuel type, air mass flow rate, fuel mass flow rate and air outlet diameter on the spray characteristics (e.g., droplet size distribution) in an annular spray burner.

The optical technique and the image processing methodology used for the present work provide several advantages over the laser techniques in terms of a higher field of view and characterization of high-density sprays. From the experimental outcomes, it is found big droplets are less affected than small ones by aerodynamic conditions. However, conditions that promote better atomization or high co-flow velocities increase the number of small droplets close to the center axis. Additionally, the spray opening angle depends on the fuel type, and at extreme co-flow velocities, the angle is narrower. On the other hand, for a particular fuel, it is found the co-flow temperature and fuel mass flow rate have a strong influence on the global Sauter mean diameter (SMD) since they affect the evaporation and the atomization processes, respectively, and especially for droplets with diameters between 5 to 16 μm. Indeed when the co-flow temperature is too high, the effect of the rest parameters is minimized. Droplet velocity is observed to be

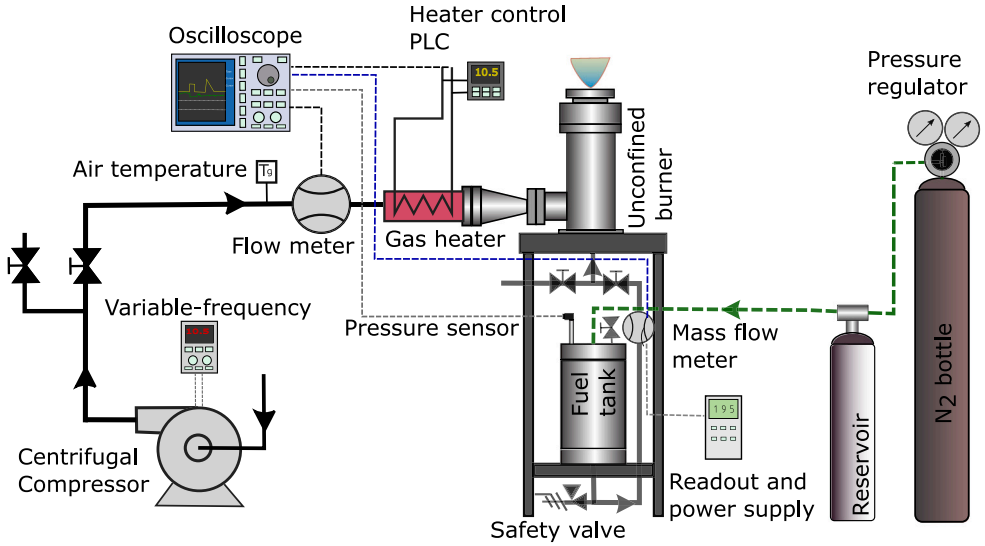

Fig. 1. Schematic representation of the high-flow and high-temperature facility.

more affected by injection pressure, droplet size, and co-flow velocity. The current paper presents an experimental investigation of the effects of varying liquid fuel type, co-flow temperature, air outlet diameter, and air co-flow rates on the spray characteristics of a pressure swirl atomizer in an annular spray burner under non-reacting conditions. The remaining manuscript first describes the experimental facilities, the experimental test conditions, the details of the optical setup, and the image processing implemented in this work. Then, the results are presented in terms of SMD, mean droplet profiles and velocity profiles at different radial positions. In addition, a comparison between estimated and measured SMD is performed. The last section summarizes the conceptual findings using Microscopic Diffused Back-Illumination technique to characterize the spray.

2. Material and methods

This section describes the facility used to carry out the measurements, test plan, optical setup, and image processing methodology.

2.1. Facility

A schematic layout of the facility used to study the spray characteristics at atmospheric conditions is presented in Fig. 1. A centrifugal blower supplies air co-flow with an air blowing-capacity of 0 - 400 $kg\,h^{-1}$ and is measured using a flowmeter. A 15 kW electric heater has been installed at the air pipeline to increase the air temperature up to 673 K, letting to investigate its effect on the spray characteristics. The air co-flow temperature is measured with K-type thermocouples at different locations and controlled by a PID module.

The fuel injection system consists of a vessel (2 L capacity) pressurized up to 5 MPa using a nitrogen bottle coupled with an extra bottle to minimize the pressure fluctuations and controlled by a pressure regulator. The vessel has multiple input connection ports to attach different sensors (e.g., thermocouples and pressure sensors). A relief valve was also installed to prevent over-pressures in the system, releasing the pressure when it exceeds 7 MPa. An electronic Coriolis mass flowmeter (Bronkhorst, CORI-FLOW) was installed in the fuel pipeline to accurately measure the fuel mass flow rate. Two solenoid valves were installed upstream of the injector to control the fuel delivery; during the injection event, the first solenoid valve permits the fuel to pass while the second one is closed. Otherwise, to interrupt fuel delivery, the first one is closed while the second one is opened, releasing the pressured fuel to the ambient to prevent the dribble effect in the injector. The fuel temperature was monitored using a K-type thermocouple just before it entered the hollow cone spray injector.

The influence of varying parameters, such as fuel mass flow rate, air mass flow rate, and co-flow temperature, on droplet size and velocity, was investigated using an annular co-flow spray burner. As illustrated in Fig. 2, the burner design is modular, allowing for easy rearrangement of the burner to simulate various air co-flow configurations. The burner was positioned vertically to provide full access to the spray/flame and prevent the gravity effect on the spray flame; moreover, no confinement and no swirled flow configurations were used throughout the experimental campaign. Furthermore, two air outlet diameters at the burner exit were tested: 19 mm and 21 mm. A cross-section of insulating material was placed between the external housing and the internal flow duct to prevent heat loss and between the co-flow channel and the fuel line, thus avoiding fuel heating. Finally, the injector was positioned flush with the air outlet diameter piece, allowing the whole spray to be registered from the nozzle tip.

All experiments were performed with a commercial pressure-swirl atomizer, which atomizes a hollow cone spray with an angle of 80°. Fig. 3 show the main components and dimensions of the injector.

Since the SMD will be calculated theoretically, the injector orifice diameter was measured from the optical microscopy images of the silicone molding of the injector, as depicted in Fig. 4. This methodology is based on the one developed to measure the internal geometry of the diesel injectors [31], which uses a specific type of silicone to introduce inside the injector and thus obtain the internal geometry. Once the molds are obtained and extracted, they are coated with gold to create an electricity conductive layer, allowing them to be imaged by Scanning Electronic Microscope (SEM) as depicted in Fig. 4. The result will not be affected by this gold deposition because the thickness of the gold coating is less than 0.1 μm. Finally, to measure the dimensions of the orifice, CAD software was used, taking into account the reference dimension (magnification factor) on the images to load them with the appropriate scale factor.

2.2. Optical setup and image processing

2.2.1. Microscopic diffused back-illumination technique

The size distribution and velocity of droplets were measured using the Microscopic diffused back-illumination (MDBI) technique, which is based on the principle of measuring the amount of light attenuated or extinguished by the interference of some features such as droplets, soot particles, and so on. In this case, when a diffused light illuminates the

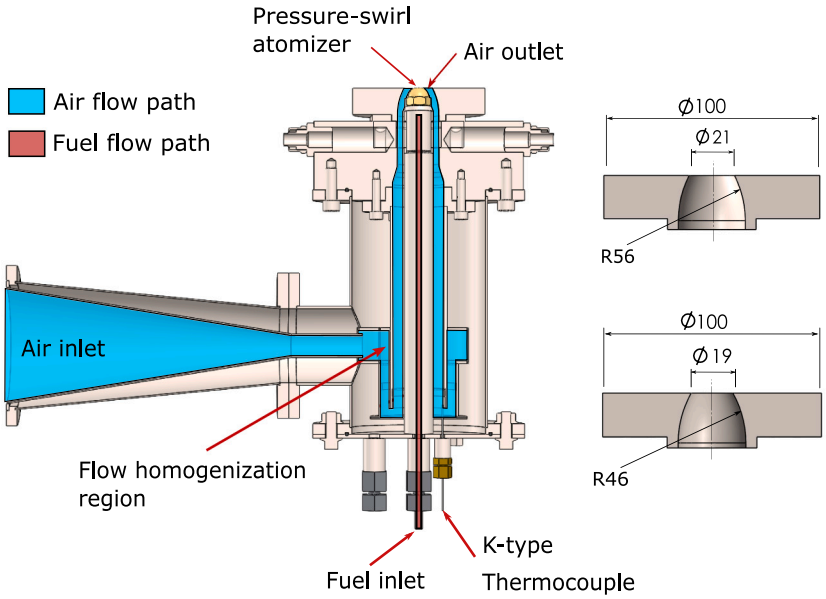

Fig. 2. Cutaway view of the annular co-flow spray burner and the air outlet diameters.

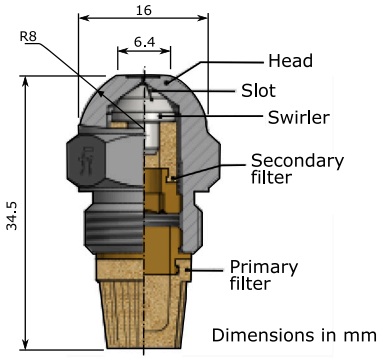

Fig. 3. Pressure-swirl atomizer, main components and dimensions.

background, the droplets and ligaments appear as black silhouettes. The MDBI setup was composed of a light source, diffuser, field lens, long-distance microscopic lens and a high-speed camera, as shown in a schematic diagram in Fig. 5. The camera (Phantom VEO640) and light source were positioned on opposite sides of the spray to set up a line-of-sight visualization arrangement. The camera was coupled with a microscopic lens (Infinity K2 Distamax) to magnify the field of view and record the droplets. A white LED unit capable of producing short and high-power light pulses at high repetition rates was used as a light source. The LED beams were directed at an engineered diffuser with a divergence angle of 20.5° and a diameter of 100 mm. Finally, the light was projected onto a Fresnel lens (focal length 67 mm) to reproduce and concentrate the diffused illumination at the central plane of the spray.

This technique was tuned to capture the microscopic spray characteristics (i.e., droplets and filaments). The camera acquisition rate was set to 1,000 frames per second (fps) to use the whole camera sensor, resulting in a resolution of 2560 × 1600 pixels. The LED energizing time was adjusted at 300 ns as a compromise between the light intensity and the recording speed. Therefore, this speed must be sufficient to "freeze" the droplet, and the illumination needs to be relatively good to provide enough contrast at the middle plane of the spray near the nozzle exit. The camera captures the light not blocked by the spray (i.e., droplets and ligaments), thus rendering the spray's liquid phase as a shadow or dark pixels in the images. Using high-speed pulsating LED as a light source makes this optical setup the best option for liquid phase visualization. This technique also captures images sharper than continuous light sources, reducing the spatial uncertainties [23,32]. This optical technique was also used to estimate the droplet velocity. It was estimated by recording two consecutive frames with a slight delay between them and controlling the background illumination by the LED pulses, similar to the principle implemented in the PIV technique. Therefore, the camera's exposure time was set to PIV mode to provide a high resetting rate of the sensor and thus minimize the time gap between the consecutive frames. Fig. 6 shows a schematic representation of the camera signal and LED pulses. Note that the LED pulse was sent at the end of frame A and the next one at the start of frame B, resulting in two frozen instants of the droplets separated by a relatively short time of 2.5 µs.

In order to optimize the optical setup, various fields of view (FOV) were assessed during the experiments to select one with suitable magnification and an adequate size. Fig. 7 shows the two magnifications evaluated; the big one has a width of 14 mm and height of 9 mm, resulting in a digital resolution of 5.6 µm per pixel, and the smaller one has a width of 3.5 mm and a height of 5.5 mm, and a digital resolution of 2.1 µm per pixel. As observed in Fig. 7.a provides a good size of the FOV, enabling recording a suitable spray length. However, it does not have enough resolution to capture the smallest droplets. Therefore, the highest magnification (i.e., the one with the digital resolution of 2.1 µm per pixel) was chosen to carry out the experiments. In addition, since the sprays show a high symmetry, as shown in Fig. 7.a, the FOV was located on the right side of the spray and the longest length vertically to register much of the spray evolution as possible.

After defining the FOV, which was located to register the first millimeters of the jet spray, registering from 2 mm above the injector tip. Details of the optical setup are summarized in Table 1.

2.2.2. *Image processing methodology*

Image processing methodology is a significant proceeding of data analysis. Images captured using the MDBI technique were processed with an algorithm to identify the droplets in the focused plane and measure their diameters and velocities. Fig. 8 presents an example of the processing steps for the frame depicted in Fig. 8.a and the steps are the following:

- Fig. 8.b: is a zoomed section of the raw spray image recorded through the MDBI technique.

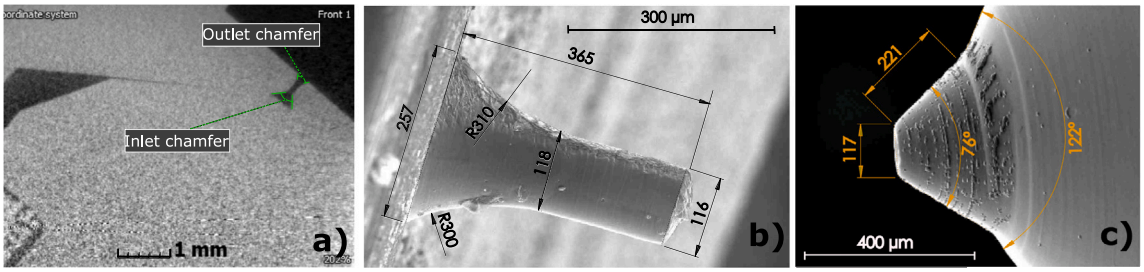

Fig. 4. Internal geometry of the pressure-swirl atomizer, X-ray at the atomizer outlet (a) and SEM images from the outlet chamfer and hole (b) and internal chamfer (c).

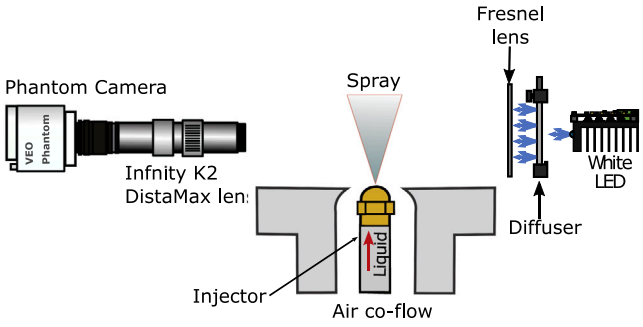

Fig. 5. Scheme of the optical set up used for the Microscopic Diffused Back Illumination.

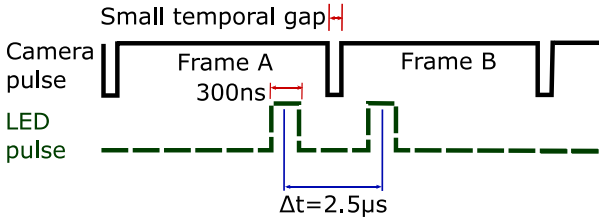

Fig. 6. Schematic representation of the camera signal and LED pulses.

Table 1
Details of the optical setup for the employed techniques.

	Microscopic Diffused Back-illumination
Camera	Phantom VEO 640
LED pulse duration	300 ns
Lens	K2 DistaMax
Frame rate	1000 fps.
Resolution	2560 × 1600
Shutter time	PIV mode
Pixels-mm ratio	465 or 2.1 µm per pixel
Repetitions	300

- Fig. 8.c: is the frame after the background subtraction (i.e., $I_{inv} = I_0 - I_{raw}$). This step removes reflections and background objects that can generate bad estimations of the spray characteristics. The subtraction was computed to obtain the particles as white features, as presented in Fig. 8.c. The background results from averaging the images captured before the injection event (I_0).
- Fig. 8.d: a rolling average was computed for resulting images from the previous step (I_{inv}) to smooth the images (I_{smooth}), i.e., reduce the image noise. Then, a subtraction was carried out ($I_{clean} = I_{inv} - I_{smooth}$) to filter out the blurred/cloudy areas, which have a low frequency and thus highlight particles with higher frequencies.
- Fig. 8.e and Fig. 8.f: a gradient estimation was calculated for each particle (I_{grad}) to identify which ones are at the middle plane of the spray (i.e., focused particles), which has a depth of field of approximately 0.032 mm. High gradients represent particles defined and focused, as shown in Fig. 8.e. Additionally, a one-step dilation method was used to move the maximum intensity from the particle borders to the center ($I_{dilgrad}$).
- Fig. 8.g: a method was established to select both the valid and focused particles and hence not consider the other ones that are not in the focus plane. They are fleeting peaks in brightness that are not particles. Thus, to determine the "good" particles at the central plane, some thresholds and the information from I_{inv}, I_{clean} and $I_{dilgrad}$. Then, the center coordinates for each particle were calculated using the local maximum intensity.

Droplet size determination

After distinguishing the valid particles in the photographs using the previous methodology, the particles bigger than 5 µm were identified and located. However, the small particles (i.e., lower than 5 µm) were not treated. The particle size captured is limited by the optical setup, which was optimized to favor the size of the FOV and record a reasonable spray length. Additionally, a threshold-based method is used to determine the pixels that belong to the droplet. Finally, multiple droplet properties, such as equivalent diameter, mass center, eccentricity, and so on, may then be calculated for these pixels using the image moment theory [33]. To characterize very small droplets, other authors are using X-ray scattering [34].

To evaluate and compare injector performance, some quantities that can account for drop dispersion characteristics must be determined. In many cases, a mean representative diameter and a variation value around it are appropriate for the application. Therefore, different mean diameter definitions are reported in the literature, each accounting for a specific effect. The Sauter mean diameter (SMD), often employed in combustion applications because it is most related to evaporation and combustion rates [35], is used here and calculated as follows,

$$SMD = \frac{\Sigma_{i=1}^{N} d_i^3}{\Sigma_{i=1}^{N} d_i^2} \tag{1}$$

where d is the droplet diameter and N is the total number of valid droplets recorded. Additionally, different theoretical correlations for pressure swirl atomizers have been established; three of the most well-known correlations were developed by Radcliffe [36], Jasuja [37], and Lefebvre and McDonell [38]:

$$SMD_{Radcliffe} = 7.3\sigma_l^{0.6}\nu_l^{0.2}\dot{m}_l^{0.25}\Delta P^{-0.4} \tag{2}$$

$$SMD_{Jasuja} = 4.4\sigma_l^{0.6}\nu_l^{0.16}\dot{m}_l^{0.22}\Delta P^{-0.43} \tag{3}$$

$$SMD_{Lefebvre} = 2.25\sigma_l^{0.25}\mu_l^{0.25}\dot{m}_l^{0.25}\Delta P^{-0.5}\rho_{air}^{-0.25} \tag{4}$$

where σ_l is the liquid surface tension, μ_l and ν_l are the dynamic and kinematic liquid viscosities, respectively; $\dot{m}_l$ is the liquid mass flow rate, ΔP is the pressure drop across the spray nozzle and ρ_{air} is the surrounding air density.

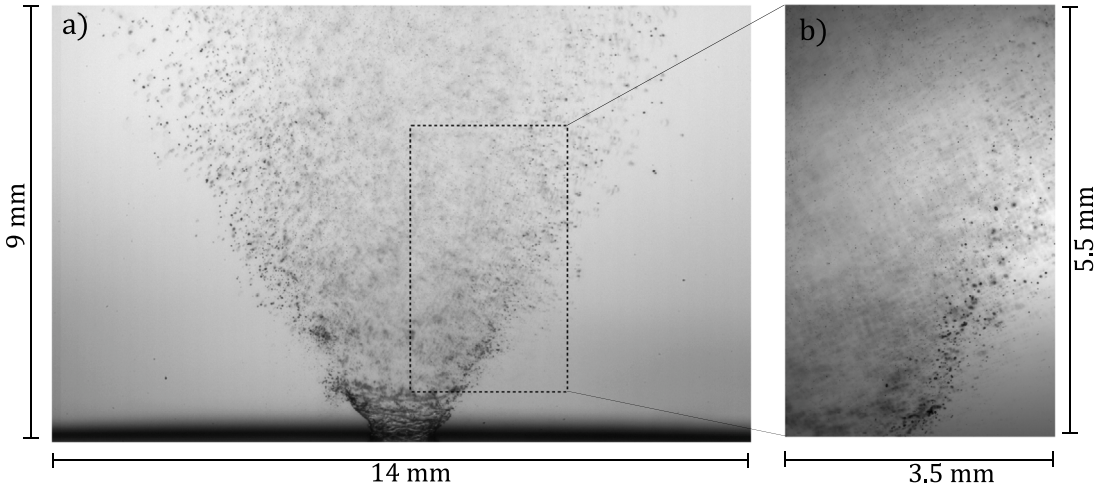

Fig. 7. Two FOVs with different digital resolution; 5.6 μm per pixel (a) and 2.1 μm per pixel (b). The frame shown is a n-Dodecane spray at air surrounding temperature of 328 K, air mass flow rate of 13.6 kg h^{-1} and fuel mass flow rate of 189.54 mg s^{-1}.

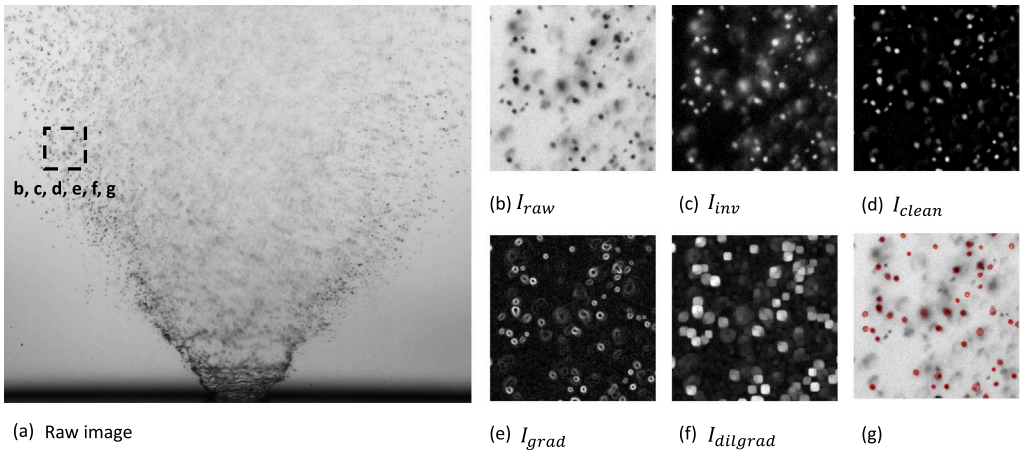

Fig. 8. (a) Raw image of the n-Dodecane spray jet at an injection pressure of 1.1 MPa, air flow of 28.5 kg h^{-1} and air temperatures of 328 K using MDBI technique and FOV of 14 mm × 9 mm. The dashed rectangle in the figure illustrates the location of the next images, only to appreciate the procedure easily. (b) Section of the raw image. (c) Image with background subtraction and inverting of the pixels. (d) Smoothing background subtraction. (e) gradient step for each particle. (f) Dilation step to move the maximum intensity of the gradient. (g) focused particles.

Droplet tracking

After separating the "good" droplets from the fake ones, it is necessary to find the most likely assignments that match each droplet in the previous frame with its counterpart in the current one, which is not always trivial. The correct match for a droplet is not always the one closest in the distance, and some droplets disappear or are introduced with each new frame, leaving droplets without counterparts. Therefore, for this task, the Python package Trackpy was used, which was developed by Allan et al. [39]. At its basic level, this tracking algorithm takes each particle in the previous frame and tries to find it in the current one, requiring knowing where to look for it. The basic algorithm (Crocker & Grier [40]) was developed to track particles undergoing Brownian diffusion, which ideally means that a particle's velocity is uncorrelated from one frame to the next. As a result, the best prediction for where a particle will move is that it will be close to its most recent position, as shown in Fig. 9.

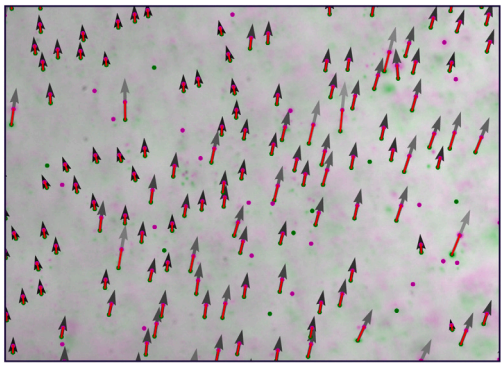

Fig. 9. Droplet trajectories generated from MDBI images. The frame shown is a n-Dodecane spray, for an air mass flow of 11.9 kg h^{-1}, fuel mass flow of 135 mg s^{-1} and air surrounding temperature of 328 K.

2.2.3. Fuel properties and test plan

The MDBI technique was carried out for a wide range of operating conditions summarized in Table 2. These conditions include three air co-flow temperatures (328, 373 and 423 K) and nine global equivalence ratios (which are directly related to air mass flow rate, injection pressure, and fuel type) for each air outlet diameter.

The co-flow velocity was theoretically calculated at the burner outlet as

$$V_{co-flow} = \frac{\dot{m}_{air}}{A \cdot \rho_{air}} \left[\frac{m}{s}\right] \quad (5)$$

Table 2
Test conditions matrix.

Parameter	Value
Fuel mass flow rate ($\dot{m}_l$) [mg s^{-1}]	(130, 159, 187.6)[a] (130.8, 159.83, 188.89)[b] (131.23, 160.4, 189.54)[c]
Air mass flow rate ($\dot{m}_{air}$) [kg h^{-1}]	11.9, 13.6, 15.6
Global equivalence ratio (ϕ_{global})	0.45, 0.52,0.55, 0.6, 0.63, 0.65, 0.73, 0.75, 0.86
Co-flow temperature ($T_{co-flow}$) [K]	328, 373, 423
Air outlet diameter ($\varnothing_{air}$) [mm]	19 and 21

[a]n-Heptane.
[b]n-Decane.
[c]n-Dodecane.

Table 3
Physical and chemical properties of the fuels. Most of the properties were extracted from the NIST database at normal temperature and pressure (i.e., 293.15 K and 1 atm) [42]. Laminar flame speed values were reported in previous works at 400 K, at 1 atm, and stoichiometric equivalence ratio [43,44].

Properties	n-Heptane	n-Decane	n-Dodecane
Formula	C_7H_{16}	$C_{10}H_{22}$	$C_{12}H_{26}$
Density (ρ_l) [kg m^{-3}]	683.94	730.53	749.5
Dynamic viscosity (μ_l) [Pa s]	0.00041	0.00091	0.00149
Surface tension (σ_l) [N m^{-1}]	0.0206[a]	0.0238[a]	0.0254[a]
Normal Boiling point [K]	371.53	447.27	489.3
P_v [kPa]	160[b]	16,5[b]	3.8[b]

[a]Along the saturation curve.
[b]At 387 K.

where $\dot{m}_{air}$ is the air mass flow rate, A is the area of the cross-section at the burner exit, and ρ_{air} is the air density. Note that co-flow velocity is influenced by varying the air co-flow temperature, which is changed in this study (see Table 2), resulting in a wide range of velocities that cover from 7.5 to 20.5 m s^{-1}.

The operating conditions summarized in Table 2 were tested for three hydrocarbon fuels: n-Heptane, n-Decane, and n-Dodecane. The fuels were chosen to cover a wide range of physical properties (summarized in Table 3), including density, viscosity, and surface tension, which influence the atomization (i.e., SMD), along with vapor pressures (P_v) and normal boiling temperatures, which impact the vaporization of the fuel. n-Heptane is the most volatile fuel, followed by n-Decane and then n-Dodecane; which has a higher normal boiling point than other two fuels. Similar fuel comparison has been used in the literature to cover a wide range of properties [41].

3. General considerations

The raw images captured using the MDBI technique are shown in Fig. 10, with a FOV of 3.5 × 5.5 mm and positioned on the right side of the spray, regarding the spray axis (see Fig. 7). Consider that this technique is based on recording two consecutive frames with a short delay to detect droplet displacement and thus measure droplet velocity.

Fig. 11 shows a scatter representation of the droplets captured using this technique at the first millimeters of the spray for all fuels at given operating conditions. From this, it is clear that the n-Heptane fuel produces the most droplets with the smallest diameters, followed by n-Decane and n-Dodecane. This trend will be further analyzed in the results section. Fuel spray presents a complex heterogeneous distribution, with droplets ranging from 2 to 100 µm, and with most of the droplets and mainly the big ones at the spray borders, which is expected by the hollow spray pattern of the pressure-swirl atomizer. Contrary, most of the small droplets were close to the spray axis since the droplets are expelled from the injector with a spray opening angle of 80°, forcing them to interact quickly with the air co-flow, which drags

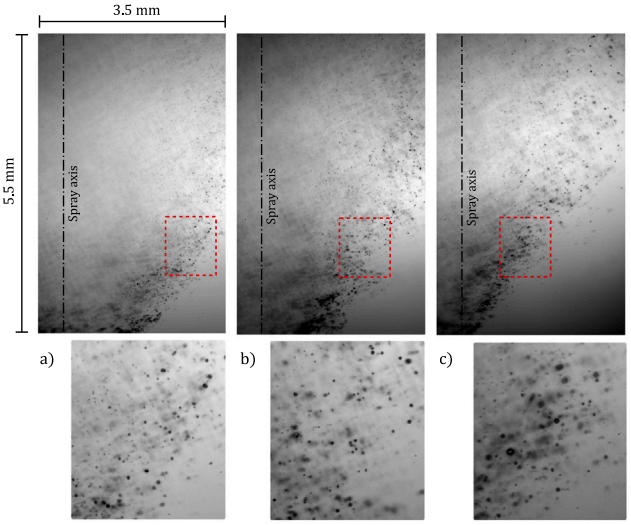

Fig. 10. Raw images at given conditions for the three fuels: n-Heptane (a), n-Decane (b), and n-Dodecane (c). The frames shown are sprays with an air surrounding temperature of 423 K, a velocity of 12.6 m s^{-1}, a global equivalence ratio of 0.6 and an air outlet diameter of 21 mm.

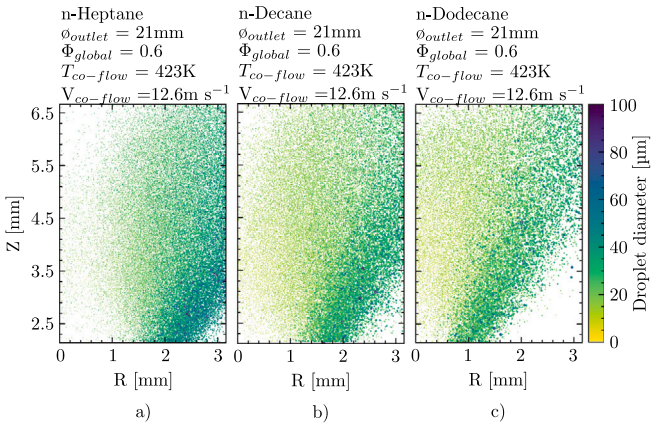

Fig. 11. Schematic representation of the droplet size at fixed conditions for the three fuels: n-Heptane (a), n-Decane (b), and n-Dodecane (c).

the small ones to this region. Finally, Fig. 11 exhibits that the lighter the fuel, the spray opening angle and the number of droplets increase.

The MDBI technique was used to record 300 pairs of consecutive frames, allowing statistical analysis to calculate mean droplet diameter, Sauter Mean Diameter (SMD), and mean velocities. Therefore, the frame domain has been split into cells to calculate a specific parameter in each one. Fig. 12 shows the SMD calculate by means of Eq. (1), in each cell for the three fuels at the same operating conditions, evidencing that most of the big droplets are at the spray borders and the heavier fuel (n-Dodecane) produces the biggest droplets, followed by n-Decane and then n-Heptane.

The individual droplet velocity is calculated for the droplets found in each pair of images. The values of all captured droplets (i.e., of all picture pairs) in the region of interest (e.g., a cell) are used for calculating average parameters, etc. The droplet velocity was represented as the SMD, i.e., by determining the mean droplet velocity for each cell, as can be seen in Fig. 13, where is also shown the standard deviation. The higher standard deviation is observed at the spray borders, where most of the droplets are located but with several different sizes and velocities.

The data shown in the following sections correspond to velocity in the cells at a certain height, resulting in a droplet velocity profile at

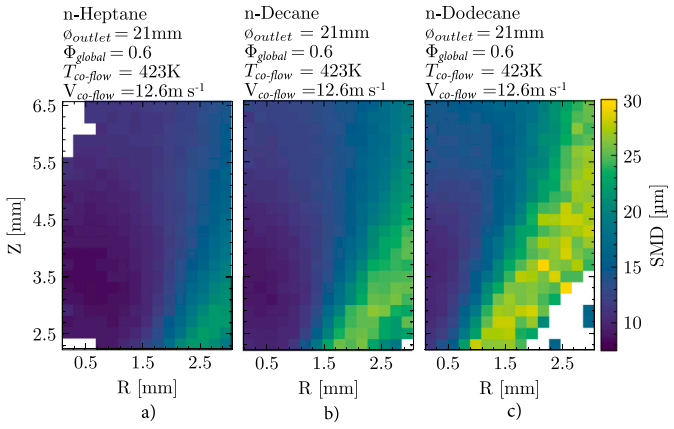

Fig. 12. Calculation of the SMD for each cell and fuel at the same operating conditions for the three fuels: n-Heptane (a), n-Decane (b), and n-Dodecane (c). White cells represent the regions that do not overcome the threshold of a least 20 droplets to conduct the statistics.

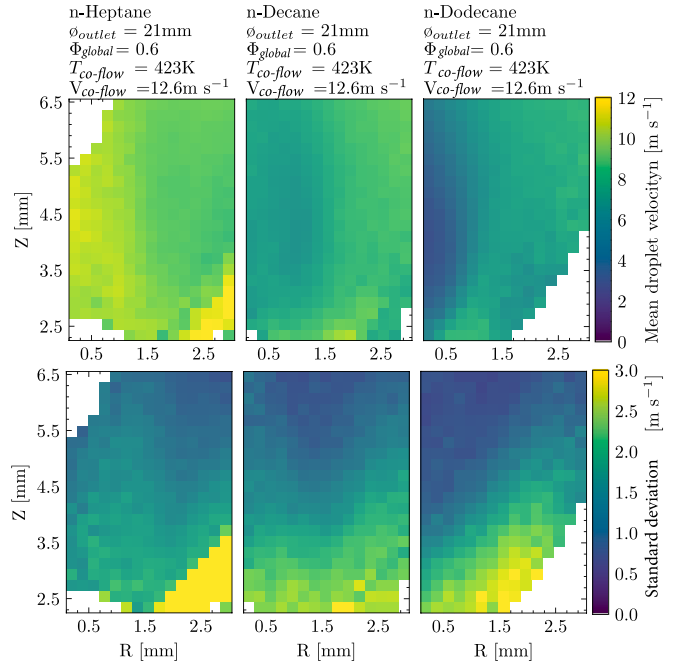

Fig. 13. Mean droplet velocity and standard deviation for each cell and the three fuels at co-flow temperature of 423 K and co-flow velocity of 12.6 m s^{-1}.

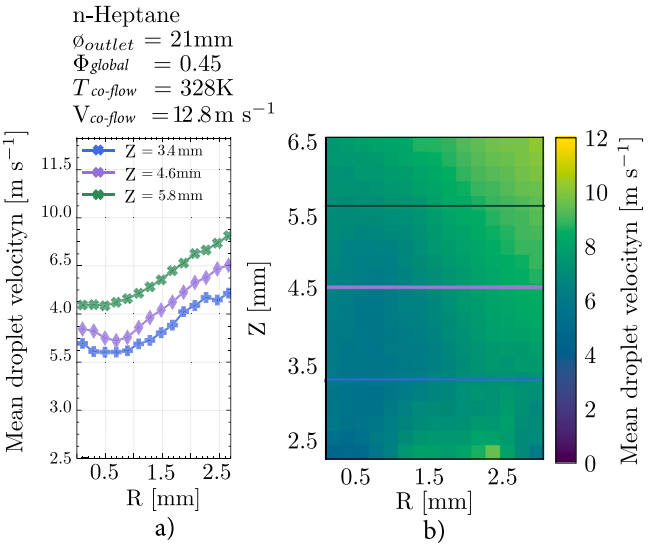

Fig. 14. Example of velocity profiles at different heights above the burner (a) and mean droplet velocity calculated for each cell for the n-Heptane fuel (b).

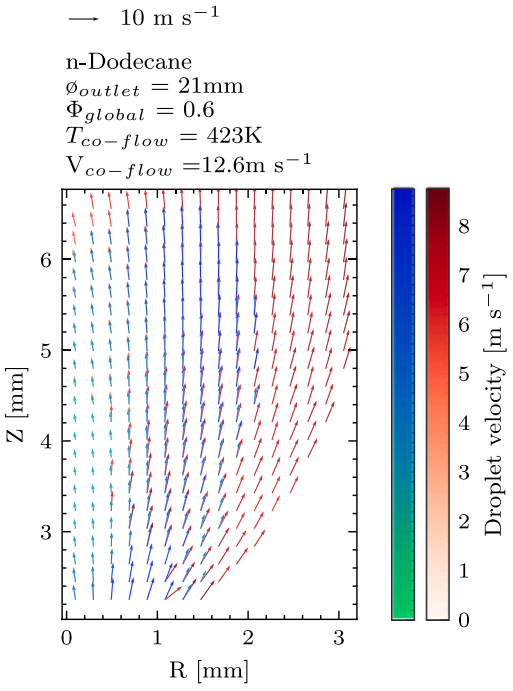

Fig. 15. Droplet trajectories for n-Dodecane fuel; red arrows represent the trajectory of droplets with a diameter higher than 12 μm and blue or green arrows diameters lower than 12 μm. (For interpretation of the references to color in this figure legend, the reader is referred to the web version of this article.)

that specific height, as the example shown in Fig. 14. From this plot, it is observed that as the height above the burner increases, the mean droplet velocity increases, which is caused by the high velocity of the air co-flow that accelerates them (the air co-flow velocity is higher than droplets). Additionally, it is exhibited that the droplets are expelled from the injector with significant velocity. They slow down as they move through to the surrounding air and recirculation zone formed at the injector tip, then droplets are accelerated again as they enter to the co-flow region.

Before discussing the results, it is important to mention relevant facts, such as the droplet trajectory behavior, regarding its size, as illustrated schematically in Fig. 15. This behavior is due to the centrifugal movement inside the atomizer that forces the liquid to be expelled in a hollow cone pattern with most droplets at the spray borders and relatively few at the core zone (see Fig. 11). The droplets in the spray core are mainly small and are more influenced by the air co-flow that drives them to follow its streamline due to their small Stokes numbers. In Fig. 15, both green and blue arrows represent the trajectory and velocity of the small droplets (diameters below 12 μm). Contrary, the aerodynamic conditions less influence the big drops with higher Stokes numbers, which follow their ballistic trajectories, as observed in Fig. 15, where red arrows represent the velocities and trajectories of the big droplets (droplet diameters above the 12 μm).

Since the droplet velocity measurements were performed close to the injector tip, aerodynamics influenced them. To further understand the following results, a small analysis of the aerodynamic conditions near the exit of the burner and close to the injector tip is presented in Appendix.

4. Results and discussion

The effects of the co-flow conditions, fuel type, and air outlet diameter on droplet size and droplet velocity are presented in this section. For simplicity, the results in this section are given in terms of SMD and velocity profiles at different heights. Note that SMD presented in this section was calculated for droplets between 2 and 3.5 mm above the injector tip to avoid the opening spray angles differences between the fuels (see Fig. 12).

4.1. Effect of air mass flow rate and fuel mass flow rate on the droplet size and velocity

Fig. 16 shows the influence of varying the air mass flow rate and fuel mass rate on the SMD for the n-Decane fuel at a co-flow temperature of 328 K. For a given fuel mass flow rate, Fig. 16.a shows that increasing the air mass flow rate (i.e., co-flow velocity) decreases slightly the SMD, which is likely due to enhancement of the droplet evaporation process. In addition, since measurements were performed very close to the burner exit, 2 mm above it, the differences are not quite noticeable. Previous research [13] found a different behavior, e.g., an increase in mean droplet size due to the evaporation of the smallest droplets by increasing the air mass flow rate; this effect will be detailed in the following sections. Fig. 16.b exhibits that the SMD reduces substantially as the fuel mass flow rate increases because it implies higher pressure drop through the nozzle orifice, which improves the atomization process, producing smaller droplets resulting in a lower global SMD.

Fig. 17.a depicts the effect of varying the air mass flow rate on droplet velocity for a constant fuel mass flow rate and n-Decane fuel. The mean droplet velocity profiles experience a dramatic rise as the radial position increases, which is expected due to the spray pattern that promotes a high number of droplets at the outer edge of the spray (mainly big droplets with high Stokes numbers). Surprisingly, increasing the air mass flow rate, the mean droplet velocity decrease between the radial position of 0 and 1.5 mm. This behavior is more evident close to the spray centerline; this behavior is due to the recirculation zone formed close to the injector tip, which intensifies as the co-flow velocity increases, as is shown in Fig. A.29. On the other hand, the velocity profiles are almost identical after a radial distance of 1.5 mm, with slightly higher droplet velocity values for the highest air mass flow rate, which accelerated the droplets because the spray opening angle is wide and the droplets immediately interact with the air co-flow.

The influence of varying the fuel mass flow rate on the droplet velocity was analyzed at a constant air mass flow rate of 11.9 $kg\,h^{-1}$, as presented in Fig. 17.b. The mean droplet velocities increase as the fuel mass flow rates increase; this is attributed to an increase in droplet ejection velocity caused by increasing the injection pressure and thus the fuel mass flow rate (the droplet ejection velocity is directly proportional to the injection pressure). Regarding the mean velocity profiles for the case of the 188.9 $mg\,s^{-1}$, it exhibits a drastic rise after the radial position at 1.6 mm, which correspond to the droplets at the spray borders, most with big sizes and expelled at high velocity from the spray. Alsulami et al. [13,45] conducted similar experiments using a pressure swirl nozzle and an annular spray burner, reporting similar trends in the effect of the fuel mass flow rate on both droplet size and droplet velocity.

4.1.1. Effect of co-flow temperature on the droplet size and velocity

Since the air temperature significantly influences the droplet size, the effect of varying the co-flow temperature on the SMD was investigated, as shown in Fig. 18.a. For a constant air mass flow rate of 11.9 $kg\,h^{-1}$ and a given fuel mass flow rate (e.g., 130.8 $mg\,s^{-1}$), increasing the co-flow temperature results in a significant reduction in the SMD caused by the enhancement in the droplet evaporation. In addition, there is an SMD difference between the different fuel mass flow rates due to the variation in the injection pressure and its effect on the atomization quality. This difference becomes lower at the highest temperature since its dominant influence on droplet evaporation over the atomization quality. However, it is important to note that the previous trend is likely affected by the co-flow velocity: increasing the co-flow temperature reduces the air density, and therefore the co-flow velocity increases (9.8, 11.1 and 12.6 $m\,s^{-1}$ for the co-flow temperatures 328, 373, and 423 K, respectively).

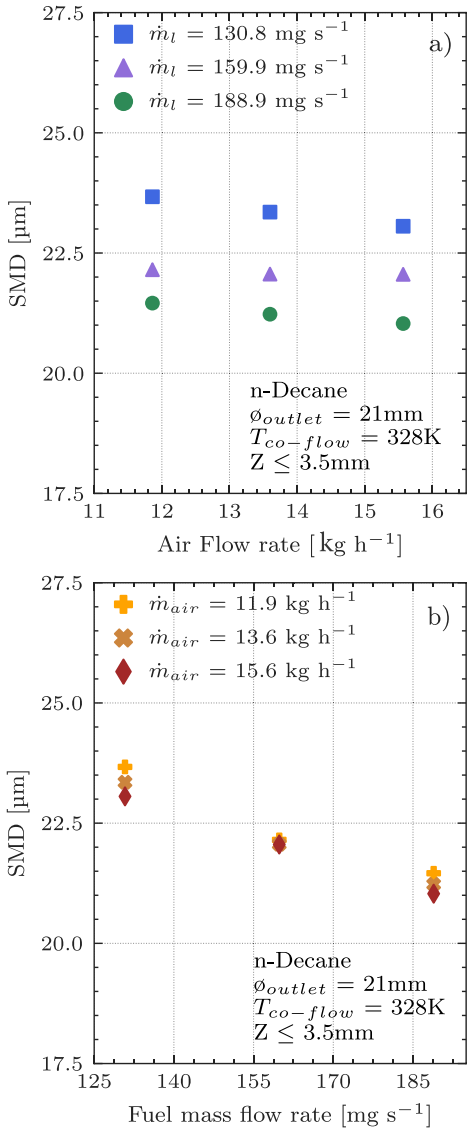

Fig. 16. Variation of SMD with the air mass flow rate (a) and fuel mass flow rate (b) for n-Decane fuel and at a given air co-flow temperature of 328 K.

To isolate the effect of the co-flow temperature on SMD, Fig. 18.b was introduced, where it can be seen that, for a constant air co-flow velocity (e.g., 13 $m\,s^{-1}$), increasing the co-flow temperature reduces the SMD substantially. This trend is due to the enhancement in the droplet vaporization rate by increasing the co-flow temperature, resulting in an SMD reduction [46]. Furthermore, for the co-flow temperatures of 328 and 373 K, increasing the co-flow velocity reduces the SMD because increasing it enhances the fuel jet breakup, resulting in smaller droplets and, therefore, lower SMD values (see Fig. 18.b). However, the previous trend is not observed with the co-flow temperature of 423 K, likely because this high co-flow temperature accelerates droplet evaporation. Thus, most of the smallest droplets are evaporated, keeping the SMD values practically constant, independent of the co-flow velocity. To further understand why SMD decreases as co-flow temperature increases,

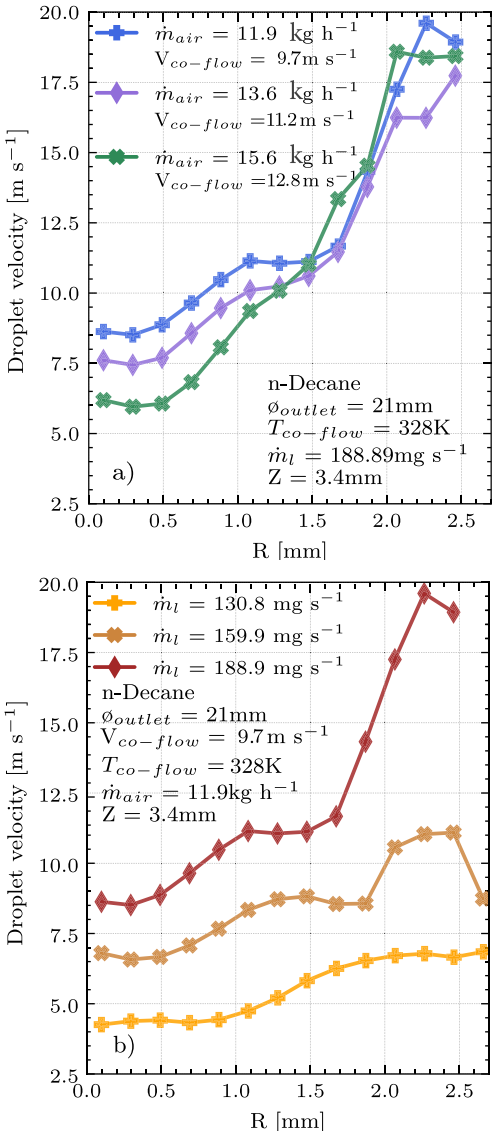

Fig. 17. Droplet velocity profiles at the height of 3.4 mm for different air mass flow rates (a) and different fuel mass flow rates (b), both for n-Decane fuel and a fixed air co-flow temperature of 328 K.

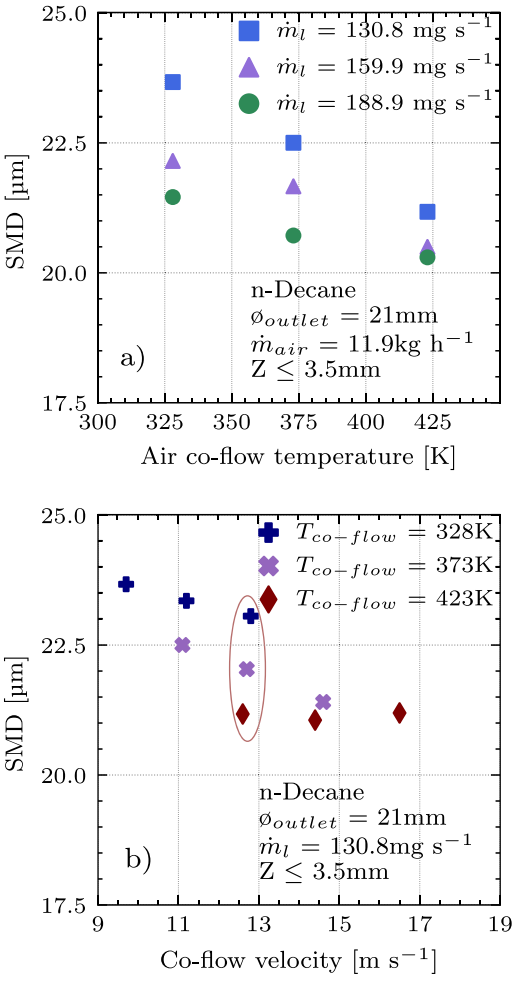

Fig. 18. Variation of SMD with the air co-flow temperature (a) and co-flow velocity (b) for n-Decane fuel.

the droplet size distributions for each fuel are shown in Fig. 19 to support the facts previously stated.

Increasing the co-flow temperature for each fuel enhances the evaporation process, affecting principally the smallest droplets and resulting in a general reduction in the number of droplets. Furthermore, it is worth noting that for the n-Decane and n-Dodecane fuels, the effect of increasing the co-flow temperature is more evident in droplets with small diameters (i.e., lower than 18 µm). For the case of the n-Heptane fuel, although the more significant effect is observed for the smaller droplets, there is also a noticeable effect for big ones (i.e., higher than 18 µm), which is due to the physical properties of the fuel, mainly the higher volatility (represented by the fuel vapor pressure in Table 3). Finally, Fig. 19 exhibits that n-Heptane fuel produces smaller droplets than the other two fuels, increasing the quantity of the droplets.

Various velocities profiles at different co-flow temperatures for two different fuel mass flow rates at a constant air mass flow rate are presented in Fig. 20 to investigate the effect of the co-flow temperature on droplet velocity. As shown in Fig. 20, the mean droplet velocities increase as the co-flow temperatures are increased. For a given air mass flow rate, increasing the co-flow temperature leads to a reduction of

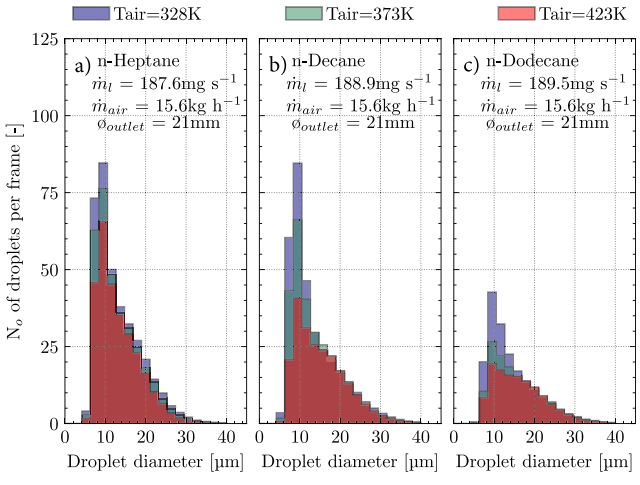

Fig. 19. Mean droplet distribution variation per frame with the co-flow temperature for the three fuels: n-Heptane (a), n-Decane (b) and n-Dodecane (c) at the same operations conditions.

the air density, which results in an increment of the co-flow velocity since the cross-section of the burner exit was kept constant. The Table 4 summarized the theoretical co-flow velocities per each condition:

Table 4
Theoretical co-flow velocities.

Air mass flow rate	Diameter	Co-flow temperature		
		328K	373K	423K
11.9 kg h^{-1}	19	12.2 m s^{-1}	13.9 m s^{-1}	15.7 m s^{-1}
	21	9.7 m s^{-1}	11.1 m s^{-1}	12.6 m s^{-1}
13.6 kg h^{-1}	19	14 m s^{-1}	15.9 m s^{-1}	18.1 m s^{-1}
	21	11.2 m s^{-1}	12.7 m s^{-1}	14.4 m s^{-1}
15.6 kg h^{-1}	19	16 m s^{-1}	18.2 m s^{-1}	20.6 m s^{-1}
	21	12.8 m s^{-1}	14.6 m s^{-1}	16.5 m s^{-1}

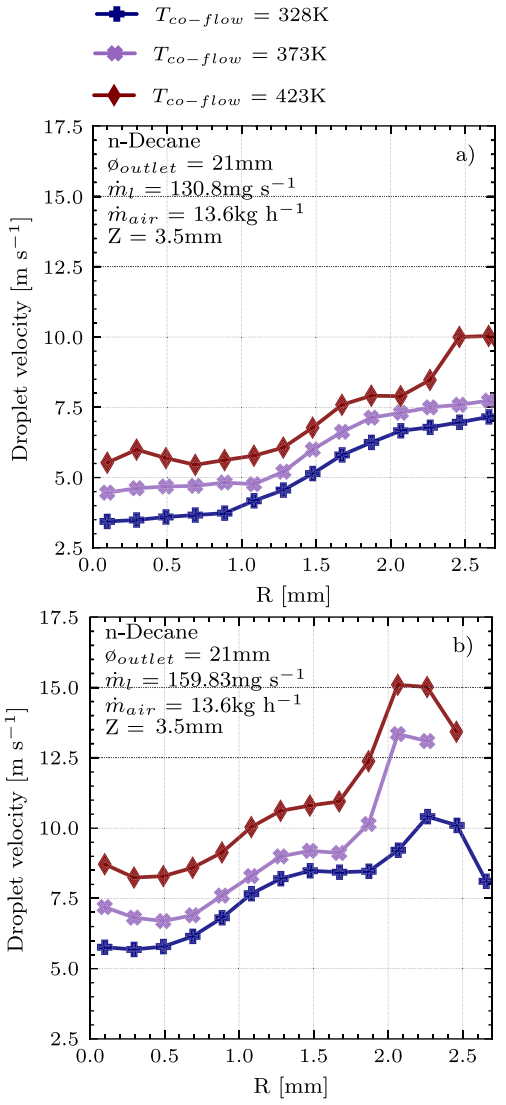

Fig. 20. Mean radial profile profiles of droplet velocities for two fuel mass flow rates of 130.8 (a) and 159.83 mg s^{-1} (b) for n-Decane fuel.

Fig. 20 also shows that increasing the fuel mass flow rate increases the mean droplet velocity, which is generated by the increase of the injection pressure, which enhances the droplet ejection velocity. Please note that the velocities profiles displayed correspond to a height of 3.5 mm above the injector tip and the injection pressures were approximately 0.97 and 1.53 MPa for 130.8 and 159.83 mg s^{-1}, respectively.

4.1.2. Effect of fuel type on the droplet size and velocity

Fig. 21 exhibits the influence of the fuel type on SMD, in which the fuels show different droplet sizes for a constant fuel mass flow

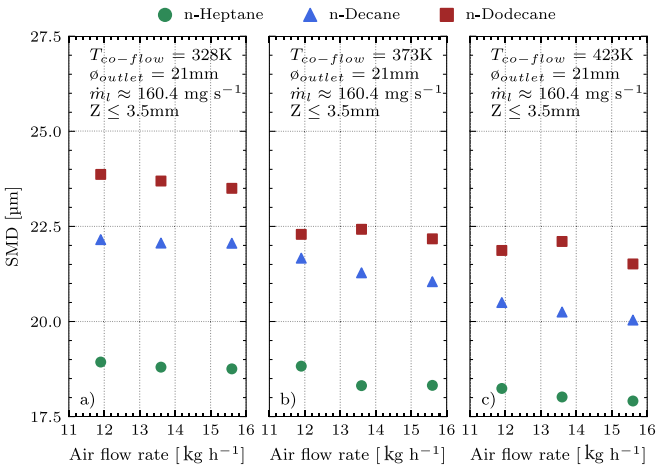

Fig. 21. Effect of the fuel type on SMD at different co-flow temperatures of 328 (a), 373 (b) and 423 K (c). The injection pressures for each fuel required to achieve the fuel mass flow rate of ≈ 160.4 mg s^{-1} were: 1.58, 1.53, 1.33 MPa for n-Heptane, n-Decane, n-Dodecane, respectively.

rate, with n-Dodecane presenting the largest droplet sizes of the group, followed by n-Decane and then far distant by n-Heptane. This variation is due to the difference in the physical properties, specifically in density, viscosity, and surface tension. Since n-Dodecane has the highest viscosity, density and surface tension (see Table 3), it generates droplets with relatively big sizes compared to n-Decane and n-Heptane. These physical properties influence the global SMD, as was reported in three well-known correlations to predict the global SMD in pressure swirl atomizers [36–38]. Fig. 21 also shows the effect of the air co-flow temperature on the SMD, as was already detailed.

The droplet velocity profiles plotted versus the radial position for the three fuels are shown in Fig. 22 at two different fuel mass flow rates: ≈ 160.4 a) and 187.6 mg s^{-1} b). Since the n-Heptane droplets are the smallest, they exhibit the highest mean droplet velocities, followed by n-Decane and then n-Dodecane. Two phenomena cause this trend: on the one hand, the droplet size differences, thus, influencing them in a different quantity, i.e., the smallest droplets are more affected by the co-flow velocity. On the other hand, since the fuels were injected at slightly different pressures to obtain the same global equivalence ratio, the ejection velocities from the injector are different. The ejection velocity is directly related to the pressure drop, i.e., the pressure difference between the ambient and the injector. The velocity profiles in Fig. 22 b) show sudden increases, which corresponds to the velocities of big droplets at the spray border and because the n-Dodecane spray angle is narrower than the other two fuels (see Fig. 11), the peak is closer to the spray axis. Furthermore, the points after peaks probably were calculated with a small number of droplets, so the statistic is not entirely accurate.

4.1.3. Diameter outlet effect on the droplet size and velocity

The effect of replacing the air outlet diameter at the burner exit on the droplet size for the three fuels at constant conditions is presented in Fig. 23. The trends shown are likely due to two factors: on the one hand, the effect of the co-flow velocity, which increases when the air outlet diameter is reduced since the air mass flow rate was kept constant, accelerating the airflow and therefore enhancing the droplet evaporation, particularly the small ones. This tendency is more notable for n-Heptane and n-Decane fuels because they produce smaller droplets than the n-Dodecane fuel, which exhibits larger droplets in size and is the less volatile fuel (see Table 3). On the other hand, due to the shape of the burner exit and the increase in co-flow velocity caused by the reduction in the cross-section at the burner exit, the airflow drags a higher number of big droplets to the spray core, displacing the

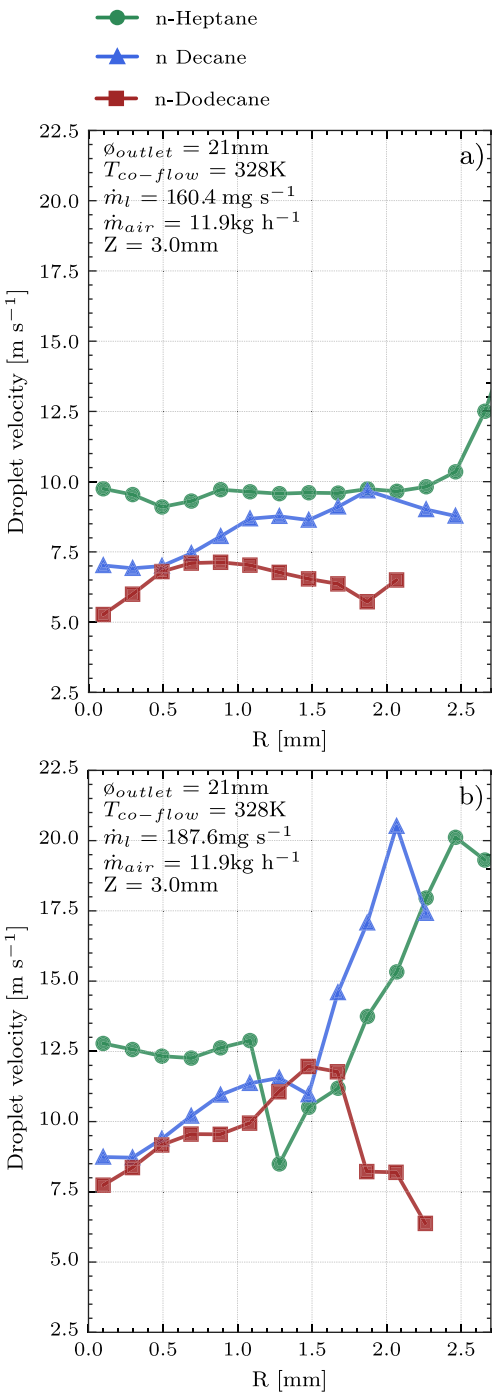

Fig. 22. Effect of the fuel type on the droplet velocity at different fuel mass flow rates of 160.4 (a) and 187.6 mg s^{-1} (b). The injection pressures for each fuel required to achieve the fuel mass flow rate of ≈ 160.4 mg s^{-1} are in Fig. 21 caption and for ≈ 187.6 mg s^{-1} were: 2.5, 2.12, 1.95 MPa for n-Heptane, n-Decane, n-Dodecane, respectively.

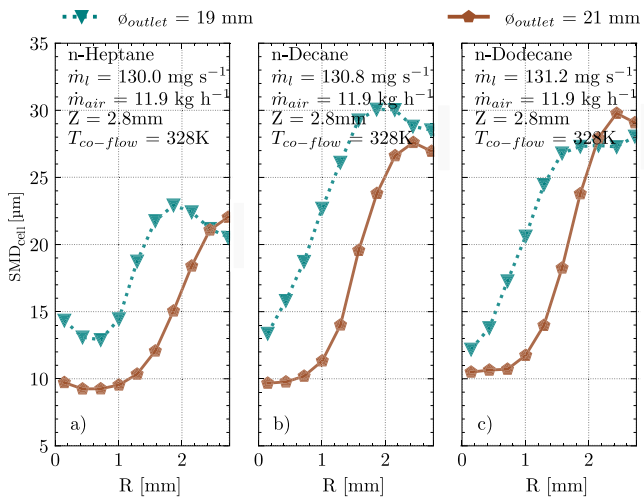

Fig. 23. Mean droplet diameter at different radial positions and a constant co-flow temperature of 328 K at the height of 2.8 mm for the fuel: n-Heptane (a), n-Decane (b) and n-Dodecane (c).

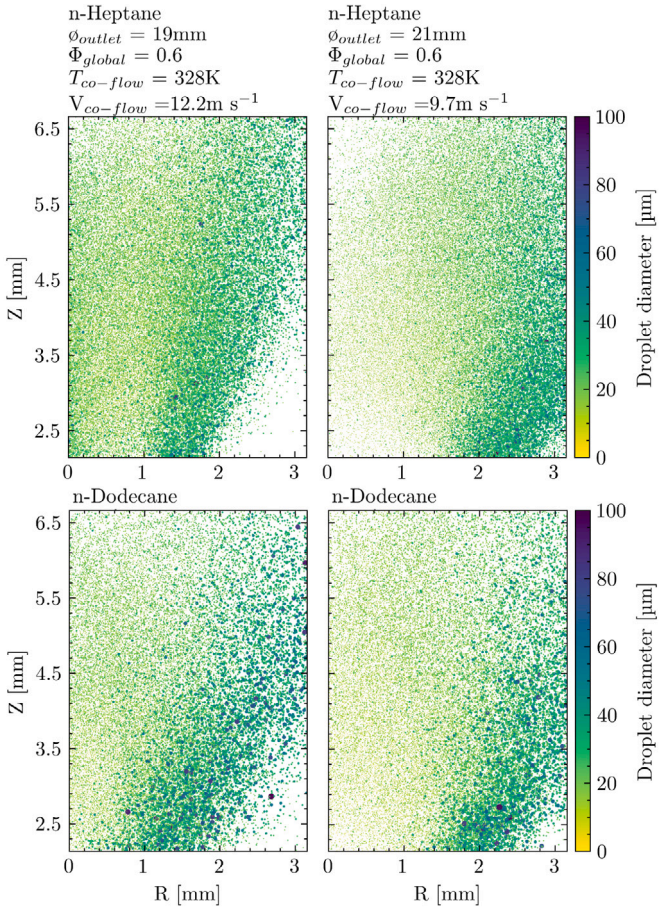

Fig. 24. Droplet representation at constant co-flow temperature for n-Heptane and n-Dodecane fuels and the two air outlet diameters of 19 and 21 mm.

SMD profiles to the left side, it for the air outlet diameter of 19 mm regards to the air outlet diameter of 21 mm. This trend is more evident for the n-Heptane fuel since it has the smallest droplets, as seen in Fig. 24, which is a schematic representation of the droplets for n-Heptane and n-Dodecane fuels for the two air outlet diameters, under identical operating conditions.

When the air outlet diameter changes from 21 mm to 19 mm, the external spray borders shift to the left side, and several droplets from the edge are dragged close to the spray axis, increasing the droplet concentration in the spray core (see Fig. 24). These tendencies result from the cross-section reduction at the burner exit, which accelerates the air co-flow, as was previously explained. Fig. 24 depicts that the n-Heptane fuel produces more droplets with a smaller diameter than the n-Dodecane fuel.

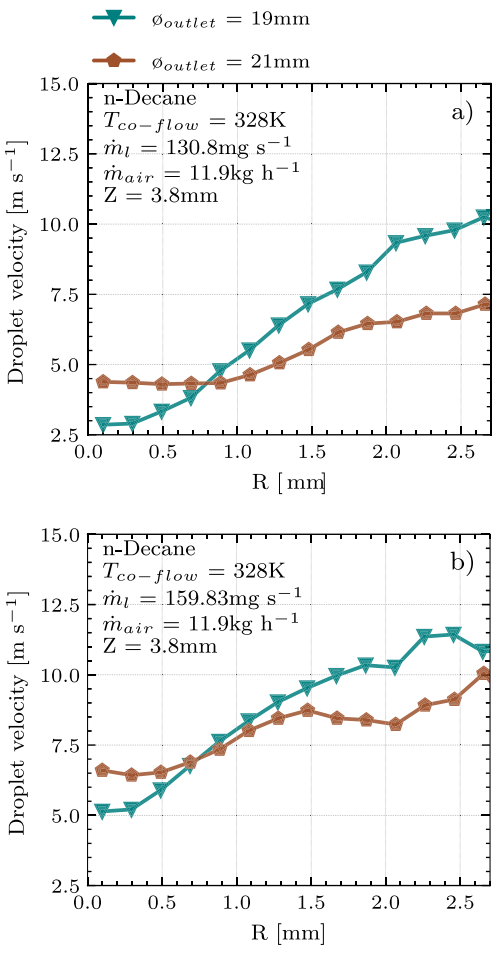

Fig. 25. Droplet velocity profiles at constant co-flow temperature of 328 K, height of 3.8 mm and two different fuel mass flow rates: 130.8 mg s^{-1} (a) and 159.8 mg s^{-1} (b). The co-flow velocities for these air mass flow rates are detailed in Table 4.

Fig. 25 shows the effect of varying the air outlet diameter of the burner on the mean droplet velocity at constant air mass flow rate and fuel mass flow rate. The mean droplet velocity increases as the air outlet diameter decreases (smaller cross-section at the burner exit) since the air mass flow rate was kept constant. However, an opposite behavior is observed between the radial positions of 0 and 0.8 mm, caused by a recirculation zone formed close to the injector tip. This region is formed by the interaction between the air stream and the injector geometry and intensified by increasing the co-flow velocity, as was explained previously.

4.2. Comparison between measured and calculated SMD

For comparing the measured and calculated SMD results, a global Sauter Mean Diameter (SMD$_{global}$) was defined as a single parameter to describe the global spray droplet size. Note that related works refer to this parameter, such as integral or overall SMD [47–49]. SMD $_{global}$ was calculated through Eq. (1). The measured SMD$_{global}$ using MDBI technique, described in Section 2.2 was compared with the SMD calculated by using the Eqs. (2)–(4). All properties used in the SMD calculations are listed in Table 3. Since the fuel injection is in the ambient, the pressure drop is measured through a pressure sensor installed upstream from the nozzle.

The measured SMD$_{global}$ (droplets between 2 and 3.5 mm) values for the three fuel mass flow rates are compared to the predicted SMDs in Fig. 26. The correlations to predict SMD have been widely used in both

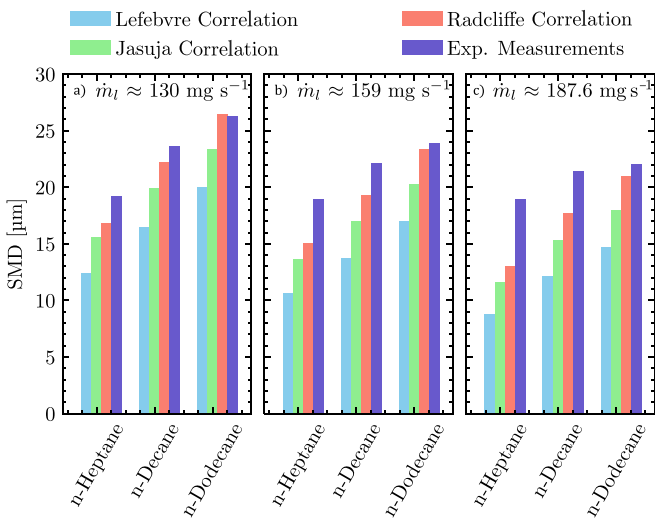

Fig. 26. Comparison between the measured and predicted SMD for a constant air mass flow rate of 11.9 kg h^{-1} and different fuel mass flow rates: 130 mg s^{-1} (a), 159 mg s^{-1} (b), and 1187.6 mg s^{-1} (c). Accurate fuel mass flow rates for each fuel are listed in Table 2.

experimental [45,50] and computational [51] studies, showing a good agreement between the measured and the predicted trends.

The differences in the physical fuel properties, particularly ones included in Eqs. (2)–(4) (density, surface tension, and viscosity), result in different droplet sizes even at almost similar fuel mass flow rates; thus, n-Dodecane exhibits the largest droplet sizes, followed by n-Decane and then n-Heptane. Amongst the fuel properties, viscosity is the property that varies more; since n-Dodecane has the highest viscosity (see Table 3), it exhibits the largest droplet size. Fig. 26 also shows that increasing the fuel mass flow rate, $\dot{m}_l$, results in an SMD decrease, which contradicts the correlations. This trend is due to the fact in our experiment; the fuel mass flow rate is increased by increasing the injection pressure, which has a more substantial effect on the global SMD than the fuel mass flow rate. Although the measured global values are higher than the predicted diameters, the predicted SMDs closely follow their trends. The differences between the measured and predicted values are lower for n-Dodecane fuel regardless of the fuel mass flow rate, showing that likely correlations are more accurate for heavier fuels. Consistently, the SMD predicted by Radcliffe's correlation is closest to the measured values, followed by Jasuja's and Lefebvre's correlations.

4.2.1. Summary

Since the figures from the previous sections only show partial sets of results, Fig. 27 is introduced as a summary to present most of the tested conditions for the air outlet diameter of 21 mm. In Fig. 27, SMD is plotted against the fuel mass flow rate and is divided by the different co-flow temperatures. Fig. 27 shows most of the facts previously stated, such as the significant influence of the fuel mass flow rate on the SMD due to the enhancement of the atomization quality. This effect is more evident for the n-Dodecane and n-Decane. As the co-flow temperature increases, the impact of fuel mass flow rate on the SMD decreases because the influence of droplet evaporation is stronger than the impact of the enhancement of the atomization quality. Increasing the co-flow temperature, regardless of fuel type, reduces the SMD due to an increase in the droplet evaporation rate. As shown Fig. 27 the effect of the air mass flow rate on the SMD is minimum, likely because the measurements were conducted quite close to the injector tip. Finally, n-Dodecane fuel presents the highest droplet diameters, followed by n-Decane and then n-Heptane; this trend is generated by the differences in the physical fuel properties, mainly density, viscosity and surface tension.

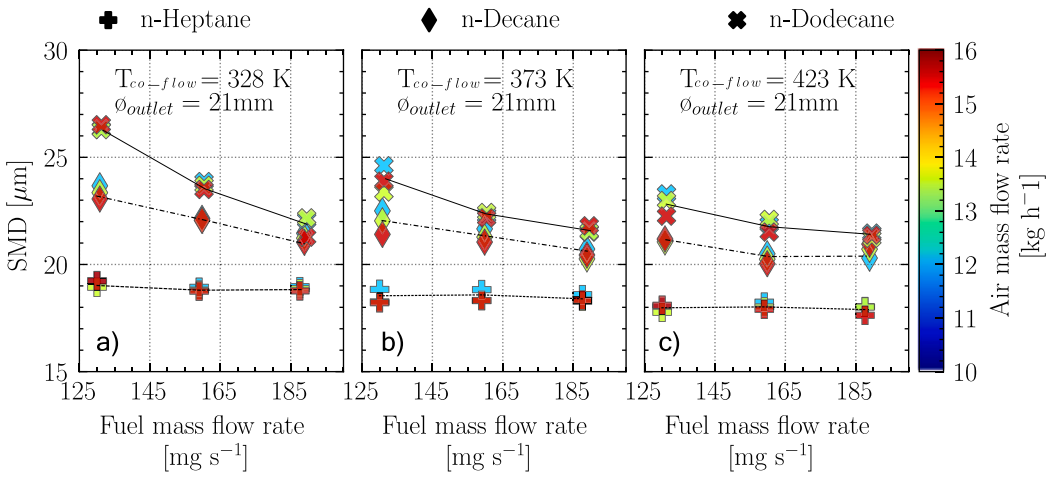

Fig. 27. SMD plotted against the fuel mass flow rate for the three fuels at different co-flow temperatures of 328, 373, 423 K. Symbols represent the fuel type and are colored by the air mass flow rate.

5. Conclusions

The purpose of this work was to investigate the effects of varying liquid fuel type, co-flow temperature, air outlet diameter and air co-flow rates on the spray characteristics of a pressure swirl atomizer in an annular spray burner under non-reacting conditions. The microscopic diffused back-illumination technique and the image processing methodology were used to measure droplet sizes and velocities of n-Heptane, n-Decane and n-Dodecane spray at different radial and axial positions. The optical setup was optimized to achieve a field of view 5.5 × 3.5 mm height and width, respectively. The field of view is relatively big, allowing the measurement of the initial droplet sizes and their velocities, i.e., close to the injector tip and after the primary breakup. In general, the trends follow the expected behavior to variations of the co-flow conditions, fuel mass flow rate and fuel type. From the results and observation, the following conclusions can be drawn:

- Because of its spray pattern, the pressure swirl injector atomizes the large droplets at the spray edge and the small ones close to the centerline. The results demonstrate that big droplets with higher Stokes numbers are less affected than the small ones by the aerodynamic conditions and follow ballistic trajectories. However, big droplets are dragged to the spray's core at certain operating conditions, mainly at high co-flow velocities.
- Isolating the effect of the air mass flow rate on the global SMD, it has been observed that it is only slightly affected, which is due to the enhancement of the droplet evaporation. The slight difference is likely because the measurements were carried out very close to the injector tip, where the influence of the air co-flow is minimal. Regarding the effect of the air mass flow rate on the droplet velocity, as it increases, the droplet velocity is increased because the co-flow accelerates the droplets since the cross-section at the burner exit was kept constant. However, this trend is contrary between 0 and 1.5 mm (radial position) due to a recirculation zone formed close to the injector tip influencing the droplet velocity. This recirculation zone is intensified by increasing the air mass flow rate.
- The influence of the fuel type on the global SMD is evident and is related to the physical fuel properties, especially the density, viscosity, and surface tension. n-Dodecane exhibits the largest droplets, followed by n-Decane and then n-Heptane. Therefore, the trajectories of the droplets behave differently, depending on their size; the co-flow stream more influences the small droplets than the big ones, which follow ballistics trajectories. n-Dodecane droplets show lower velocities since they are bigger and their ejection velocities are lower than the other two fuels because the injection pressure is lower, thus the fuel mass flow rate. The fuel type also affects the spray opening angle under the same operating conditions, with n-Heptane having the widest opening angle, followed by n-Decane and then n-Dodecane.
- For a constant fuel mass flow rate, increasing the co-flow temperature results in a significant reduction in the SMD caused by the enhancement in droplet evaporation. In addition, there is an SMD difference between the different fuel mass flow rates due to the variation in the injection pressure and its effect on the atomization quality. This difference becomes lower at the highest temperature since the influence of droplet evaporation is more dominant than the atomization effect.
- Regarding the effect of the air outlet diameter on the SMD, it has been observed that when the air outlet diameter decreases, the global SMD increases at constant operating conditions. This trend can be related to an increase in co-flow velocity, which increases the evaporation rates of the fuel droplets, particularly the smaller ones, leading to a higher global SMD. On the other hand, due to the shape of the burner exit and the increase in co-flow velocity caused by the reduction in the cross-section at the burner exit, the airflow drags a higher number of droplets of larger size to the spray core, displacing the SMD profiles to the spray axis, it for the air outlet diameter of 19 mm regards to the air outlet diameter of 21 mm. Because of reducing the air outlet diameter, the air co-flow velocity is increased. Therefore, the droplets are also accelerated, exhibiting higher droplet velocities.
- The correlations do well at predicting SMD values and the relative change of the SMD with varying the fuel mass flow rate. However, since the correlations do not consider the influence of the co-flow conditions, the current formulas do not predict the variations in the global SMD when the air mass flow rate or co-flow temperature are increased.

CRediT authorship contribution statement

Santiago Cardona: Methodology, Software, Formal analysis, Investigation, Validation, Visualization, Writing – original draft. **Raul Payri:** Funding acquisition, Data curation, Resources, Writing – review & editing. **F.J. Salvador:** Funding acquisition, Resources, Writing – review & editing. **Jaime Gimeno:** Project administration, Conceptualization, Supervision, Software, Methodology, Formal analysis, Writing – review & editing.

Declaration of competing interest

The authors declare that they have no known competing financial interests or personal relationships that could have appeared to influence the work reported in this paper.

Data availability

The data that has been used is confidential.

Acknowledgments

This research was funded by the Spanish Ministerio de Ciencias e Innovación through project reference PID2021-125812OB-C21. Part of the experimental equipment was purchased with support from Conselleria de Innovación, Universidades, Ciencia *y* Sociedad Digital of Generalitat Valenciana through grant CIPPC/2021/49. Finally, the support of Omar Huerta Cornejo, Jose E. del Rey and Carlos Gil in conducting the experiments and laboratory work is greatly appreciated.

Appendix. Aerodynamic conditions at the burner exit

This analysis comprises a basic computational simulation of the flow dynamics at the burner exit, only considering air. The results show that the air recirculation is more intense close to the injector tip, affecting the droplet velocity profiles presented in the following section. Fig. A.28 exhibits that by increasing the air mass flow rate or reducing the air outlet diameter, the recirculation zone is intensified due to the acceleration of the surrounding air stream.

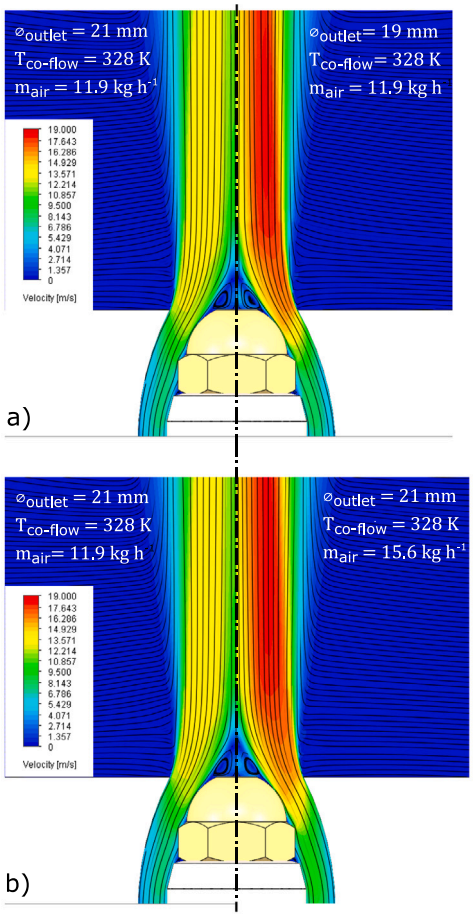

Fig. A.28. Axial velocity map at a constant co-flow temperature of 328 K, and different test conditions: two air outlet diameter a) and two air mass flow rate b).

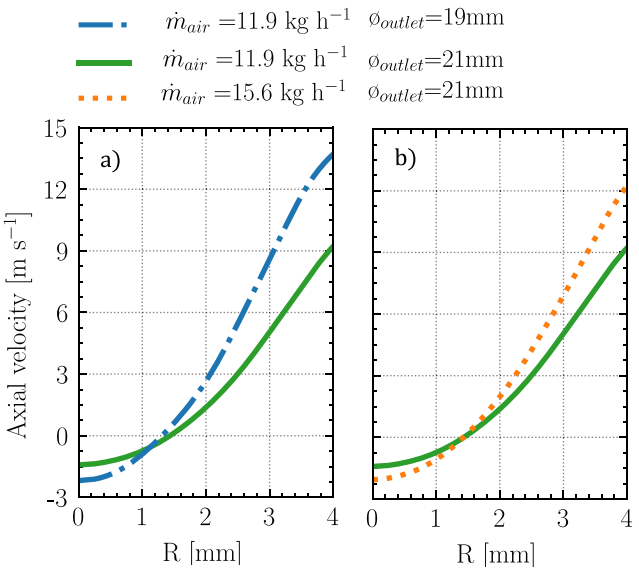

Fig. A.29. Axial velocity profile of airflow at the height of 3.8 mm, the constant co-flow temperature of 328 K, and different test conditions: two air outlet diameter (a) and two air mass flow rate (b).

Fig. A.29 represents the axial velocity profiles at the height of 3.8 mm above the injector tip, exhibiting that increasing the co-flow velocity (e.g., by an air mass flow rate increased or air outlet diameter reduction), a more intense recirculation zone is created. However, the vortex size is only slightly affected regardless of the operating condition, as seen in Fig. A.29.

Note since only air was considered in the simulation, the results show negative velocity values; it is expected that these values should change to positive velocity values with fuel injection.

References

[1] Presser C, Gupta A, Avedisian C, Semerjian H. Fuel property effects on the structure of spray flames. Symp (Int) Combust 1991;23:1361–7. http://dx.doi.org/10.1016/S0082-0784(06)80401-7, https://www.sciencedirect.com/science/article/pii/S0082078406804017.

[2] Edwards C, Rudoff R. Structure of a swirl-stabilized spray flame by imaging, laser doppler velocimetry, and phase doppler anemometry. Symp (Int) Combust 1991;23:1353–9. http://dx.doi.org/10.1016/S0082-0784(06)80400-5, https://www.sciencedirect.com/science/article/pii/S0082078406804005.

[3] G. Mcdonell, Adachi M, Samuelsen GS. Structure of reacting and non-reacting swirling air-assisted sprays. Combust Sci Technol 1992;82:225–48. http://dx.doi.org/10.1080/00102209208951821, http://www.tandfonline.com/doi/abs/10.1080/00102209208951821.

[4] Abdollahipoor B, Shirazi SA, Reardon KF, Windom BC. Near-azeotropic volatility behavior of hydrous and anhydrous ethanol gasoline mixtures and impact on droplet evaporation dynamics. Fuel Process Technol 2018;181:166–74. http://dx.doi.org/10.1016/j.fuproc.2018.09.019.

[5] Sivakumar D, Vankeswaram SK, Sakthikumar R, Raghunandan BN. Analysis on the atomization characteristics of aviation biofuel discharging from simplex Swirl atomizer. Int J Multiph Flow 2015;72:88–96. http://dx.doi.org/10.1016/j.ijmultiphaseflow.2015.02.009.

[6] Davanlou A, Lee JD, Basu S, Kumar R. Effect of viscosity and surface tension on breakup and coalescence of bicomponent sprays. Chem Eng Sci 2015;131:243–55. http://dx.doi.org/10.1016/j.ces.2015.03.057.

[7] Fisher BT, Weismiller MR, Tuttle SG, Hinnant KM. Effects of fluid properties on spray characteristics of a flow-blurring atomizer. J Eng Gas Turbines Power 2018;140. http://dx.doi.org/10.1115/1.4038084.

[8] Shum-Kivan F, Marrero Santiago J, Verdier A, Riber E, Renou B, Cabot G, et al. Experimental and numerical analysis of a turbulent spray flame structure. Proc Combust Inst 2017;36:2567–75. http://dx.doi.org/10.1016/J.PROCI.2016.06.039, https://www.sciencedirect.com/science/article/pii/S1540748916300979.

[9] Verdier A, Marrero Santiago J, Vandel A, Saengkaew S, Cabot G, Grehan G, et al. Experimental study of local flame structures and fuel droplet properties of a spray jet flame. Proc Combust Inst 2017;36:2595–602. http://dx.doi.org/10.1016/j.proci.2016.07.016.

[10] Correia Rodrigues H, Tummers MJ, van Veen EH, Roekaerts DJ. Spray flame structure in conventional and hot-diluted combustion regime. Combust Flame 2015;162:759–73. http://dx.doi.org/10.1016/j.combustflame.2014.07.033.

[11] Stårner SH, Gounder J, Masri AR. Effects of turbulence and carrier fluid on simple, turbulent spray jet flames. Combust Flame 2005;143:420–32. http://dx.doi.org/10.1016/j.combustflame.2005.08.016.

[12] Sommerfeld M, Qiu HH. Experimental studies of spray evaporation in turbulent flow. Int J Heat Fluid Flow 1998;19:10–22. http://dx.doi.org/10.1016/S0142-727X(97)10002-9.

[13] Alsulami RA, Nates S, Wang W, Won SH, Windom B. Effects of varying liquid fuel and air co-flow rates on spray characterisation of an annular co-flow spray burner. In: Proceedings of the ASME turbo expo. Vol. 4B-2019. American Society of Mechanical Engineers (ASME); 2019, http://dx.doi.org/10.1115/GT2019-90989.

[14] Friedman JA, Renksizbulut M. Investigating a methanol spray flame interacting with an annular air jet using phase-doppler interferometry and planar laser-induced fluorescence. Combust Flame 1999;2180. http://dx.doi.org/10.1016/S0010-2180(98)00136-9.

[15] Marley SK, Welle EJ, Lyons KM, Roberts WL. Effects of leading edge entrainment on the double flame structure in lifted ethanol spray flames. Exp Therm Fluid Sci 2004;29:23–31. http://dx.doi.org/10.1016/j.expthermflusci.2004.01.009.

[16] Li X, Li D, Pei Y, Peng Z. Optimising microscopic spray characteristics and particle emissions in a dual-injection spark ignition (SI) engine by changing GDI injection pressure. Int J Engine Res 2022;14680874221082793. http://dx.doi.org/10.1177/14680874221082793.

[17] Düwel I, Ge HW, Kronemayer H, Dibble R, Gutheil E, Schulz C, et al. Experimental and numerical characterization of a turbulent spray flame. Proc Combust Inst 2007;31:2247–55. http://dx.doi.org/10.1016/j.proci.2006.07.111.

[18] Verdier A, Marrero Santiago J, Vandel A, Saengkaew S, Cabot G, Grehan G, et al. Experimental study of local flame structures and fuel droplet properties of a spray jet flame. Proc Combust Inst 2017;36:2595–602. http://dx.doi.org/10.1016/j.proci.2016.07.016.

[19] Marrero Santiago J, Verdier A, Vandel A, Godard G, Cabot G, Renou B. Spray ignition and local flow properties in a swirled confined spray-jet burner: experimental analysis. In: Proceedings ILASS–Europe 2017. 28th Conference on liquid atomization and spray systems. Valencia: Universitat Politècnica València; 2017, http://dx.doi.org/10.4995/ILASS2017.2017.4674, http://ocs.editorial.upv.es/index.php/ILASS/ILASS2017/paper/view/4674.

[20] Bracho G, Postrioti L, Moreno A, Brizi G. Experimental study of the droplet characteristics of a SCR injector spray through optical techniques. Int J Multiph Flow 2021;135:103531. http://dx.doi.org/10.1016/J.IJMULTIPHASEFLOW.2020.103531.

[21] Gimeno J, Martí-aldaraví P, Carreres M, Cardona S. Experimental investigation of the lift-off height and soot formation of a spray flame for different co-flow conditions and fuels. Combust Flame 2021;233:111589. http://dx.doi.org/10.1016/j.combustflame.2021.111589.

[22] Payri R, Bracho G, Gimeno J, Moreno A. Investigation of the urea-water solution atomization process in engine exhaust-like conditions. Exp Therm Fluid Sci 2019;108:75–84. http://dx.doi.org/10.1016/j.expthermflusci.2019.05.019.

[23] Manin J, Bardi M, Pickett L, Dahms R, Oefelein J. Microscopic investigation of the atomization and mixing processes of diesel sprays injected into high pressure and temperature environments. Fuel 2014;134:531–43. http://dx.doi.org/10.1016/j.fuel.2014.05.060, https://linkinghub.elsevier.com/retrieve/pii/S0016236114005225.

[24] Payri R, Gimeno J, Cardona S, Ayyapureddi S. Measurement of soot concentration in a prototype multi- hole diesel injector by high-speed color diffused back illumination technique. SAE Technical Paper 2017-01-2255, 2017, http://dx.doi.org/10.4271/2017-01-2255.

[25] Cheng Q, Tuomo H, Kaario OT, Martti L. Spray dynamics of HVO and EN590 diesel fuels. Fuel 2019;245:198–211. http://dx.doi.org/10.1016/J.FUEL.2019.01.123.

[26] Du J, Mohan B, Sim J, Fang T, Roberts WL. Macroscopic non-reacting spray characterization of gasoline compression ignition fuels in a constant volume chamber. Fuel 2019;255:115818. http://dx.doi.org/10.1016/J.FUEL.2019.115818.

[27] Chen C, Yang Y, Wang X, Tang W. Effect of geometric and operating parameters on the spray characteristics of an open-end swirl injector. Proc Inst Mech Eng G 2019;1–11. http://dx.doi.org/10.1177/0954410018824519.

[28] Yan J, Chen T, Gao S, Lee T, Diaz E, Lee C-F. Macroscopic and microscopic characteristics of flash boiling spray with binary fuel mixtures. SAE Int J Engines 2019. http://dx.doi.org/10.4271/2019-01-0274, https://www.sae.org/content/2019-01-0274/.

[29] Manin J, Pickett LM, Crua C. Microscopic observation of miscible mixing in sprays at elevated temperatures and pressures. In: ILASS Americas 27th annual conference of liquid atomization and spray systems, Raleigh. 2015, http://www.ilass.org/2/conferencepapers/93_2015.pdf.

[30] Sukhanovskii A, Batalov V, Stepanov R. Drawbacks of GPT and IPI measurements in dense sprays. Exp Therm Fluid Sci 2019;103:29–36. http://dx.doi.org/10.1016/j.expthermflusci.2019.01.005, https://linkinghub.elsevier.com/retrieve/pii/S0894177718315395.

[31] Macian V, Bermúdez V, Payri R, Gimeno J. New technique for determination of internal geometry of a Diesel nozzle with the use of silicone methodology. Exp Tech 2003;27:39–43. http://dx.doi.org/10.1111/j.1747-1567.2003.tb00107.x, http://doi.wiley.com/10.1111/j.1747-1567.2003.tb00107.x.

[32] Payri R, Bracho G, Gimeno J, Moreno A. Spray characterization of the urea-water solution (UWS) injected in a hot air stream analogous to SCR system operating conditions. In: WCX SAE world congress experience. Vol. 1. 2019, p. 1–9. http://dx.doi.org/10.4271/2019-01-0738, https://www.sae.org/content/2019-01-0738/.

[33] Mukundan R, Ramakrishnan KR. Moment functions in image analysis: theory and applications. World Scientific; 1998, http://dx.doi.org/10.1142/3838.

[34] Kastengren AL, Ilavsky J, Viera JP, Payri R, Duke DJ, Swantek AB, et al. Measurements of droplet size in shear-driven atomization using ultra-small angle x-ray scattering. Int J Multiph Flow 2017;92:131–9. http://dx.doi.org/10.1016/j.ijmultiphaseflow.2017.03.005, http://linkinghub.elsevier.com/retrieve/pii/S0301932216305596.

[35] Lefebvre AH. Airblast atomization. Prog Energy Combust Sci 1980;6:233–61. http://dx.doi.org/10.1016/0360-1285(80)90017-9.

[36] Radcliffe A. Section D. Fuel injection. In: Design and performance of gas turbine power plants. Princeton University Press; 2015, p. 92–118. http://dx.doi.org/10.1515/9781400875603-008.

[37] Jasuja AK. Atomization of crude and residual fuel oils. J Eng Gas Turbines Power 1979;101:250–8. http://dx.doi.org/10.1115/1.3446480.

[38] Lefebvre A, McDonell V. Atomization and sprays. 2017, http://dx.doi.org/10.1016/0009-2509(90)87140-N, https://www.crcpress.com/Atomization-and-Sprays-Second-Edition/Lefebvre-McDonell/p/book/9781498736251.

[39] Allan DB, Caswell T, Keim NC, van der Wel CM, Verweij RW. Trackpy v0.5.0. 2021, https://zenodo.org/record/4682814. http://dx.doi.org/10.5281/ZENODO.4682814.

[40] Crocker JC, Grier DG. Methods of digital video microscopy for colloidal studies. J Colloid Interface Sci 1996;179:298–310. http://dx.doi.org/10.1006/JCIS.1996.0217.

[41] Payri R, Viera JP, Gopalakrishnan V, Szymkowicz PG. The effect of nozzle geometry over the evaporative spray formation for three different fuels. Fuel 2017;188:645–60. http://dx.doi.org/10.1016/j.fuel.2016.06.041.

[42] Linstrom PJ, Mallard WG. The NIST chemistry WebBook: A chemical data resource on the internet. J Chem Eng Data 2001;46:1059–63. http://dx.doi.org/10.1021/je000236i, http://webbook.nist.gov.

[43] Naik CV, Puduppakkam KV, Modak A, Meeks E, Wang YL, Feng Q, et al. Detailed chemical kinetic mechanism for surrogates of alternative jet fuels. Combust Flame 2011;158:434–45. http://dx.doi.org/10.1016/j.combustflame.2010.09.016.

[44] Kumar K, Freeh JE, Sung CJ, Huang Y. Laminar flame speeds of preheated iso-octane/O2/N2 and n-heptane/O2/N2 mixtures. J Propuls Power 2007;23:428–36. http://dx.doi.org/10.2514/1.24391, https://arc.aiaa.org/doi/abs/10.2514/1.24391.

[45] Alsulami R, Windell B, Nates S, Wang W, Won SH, Windom B. Investigating the role of atomization on flame stability of liquid fuels in an annular spray burner. Fuel 2020;265. http://dx.doi.org/10.1016/j.fuel.2019.116945.

[46] Reddy VM, Trivedi D, Kumar S. Experimental investigations on lifted spray flames for a range of coflow conditions. Combust Sci Technol 2012;184:44–63. http://dx.doi.org/10.1080/00102202.2011.615770.

[47] Im JH, Kim D, Han P, Yoon Y, Bazarov V. Self-pulsation characteristics of a gas-liquid swirl coaxial injector. At Sprays 2009;19:57–74. http://dx.doi.org/10.1615/atomizspr.v19.i1.40, http://www.dl.begellhouse.com/journals/6a7c7e10642258cc,2f2d6c0205a2559a,7d89de500980347f.html.

[48] Tratnig A, Brenn G. Drop size spectra in sprays from pressure-swirl atomizers. Int J Multiph Flow 2010;36:349–63. http://dx.doi.org/10.1016/j.ijmultiphaseflow.2010.01.008.

[49] Jedelsky J, Jicha M. Energy considerations in spraying process of a spill-return pressure-swirl atomizer. Appl Energy 2014;132:485–95. http://dx.doi.org/10.1016/j.apenergy.2014.07.042.

[50] Wei X, Yong H. Improved semiempirical correlation to predict Sauter mean diameter for pressure-swirl atomizers. J Propuls Power 2014;30:1628–35. http://dx.doi.org/10.2514/1.B35238, http://arc.aiaa.org/doi/10.2514/1.B35238.

[51] Dikshit SB, Kulshreshtha DB, Channiwala SA. Numerical analysis and empirical correlations to predict SMD of pressure swirl atomizer for small scale gas turbine combustion chamber. Int J Appl Eng Res 2018;13:4531–7.